



NAVAL POSTGRADUATE SCHOOL

MONTEREY, CALIFORNIA

THESIS

**MODEL FOR ATMOSPHERIC PROPAGATION OF
SPATIALLY COMBINED LASER BEAMS**

by

Kum Leong Lee

September 2016

Thesis Co-Advisors:

Joseph Blau
Keith Cohn

Approved for public release. Distribution is unlimited.

THIS PAGE INTENTIONALLY LEFT BLANK

REPORT DOCUMENTATION PAGE			Form Approved OMB No. 0704-0188	
Public reporting burden for this collection of information is estimated to average 1 hour per response, including the time for reviewing instruction, searching existing data sources, gathering and maintaining the data needed, and completing and reviewing the collection of information. Send comments regarding this burden estimate or any other aspect of this collection of information, including suggestions for reducing this burden to Washington headquarters Services, Directorate for Information Operations and Reports, 1215 Jefferson Davis Highway, Suite 1204, Arlington, VA 22202-4302, and to the Office of Management and Budget, Paperwork Reduction Project (0704-0188) Washington DC 20503.				
1. AGENCY USE ONLY (Leave Blank)	2. REPORT DATE Sept 2016	3. REPORT TYPE AND DATES COVERED Master's Thesis 12-01-2015 to 09-23-2016		
4. TITLE AND SUBTITLE MODEL FOR ATMOSPHERIC PROPAGATION OF SPATIALLY COMBINED LASER BEAMS		5. FUNDING NUMBERS		
6. AUTHOR(S) Kum Leong Lee				
7. PERFORMING ORGANIZATION NAME(S) AND ADDRESS(ES) Naval Postgraduate School Monterey, CA 93943		8. PERFORMING ORGANIZATION REPORT NUMBER		
9. SPONSORING / MONITORING AGENCY NAME(S) AND ADDRESS(ES) N/A		10. SPONSORING / MONITORING AGENCY REPORT NUMBER		
11. SUPPLEMENTARY NOTES The views expressed in this document are those of the author and do not reflect the official policy or position of the Department of Defense or the U.S. Government. IRB Protocol Number: N/A.				
12a. DISTRIBUTION / AVAILABILITY STATEMENT Approved for public release. Distribution is unlimited.		12b. DISTRIBUTION CODE		
13. ABSTRACT (maximum 200 words) This thesis developed a propagation model that can be used to investigate the performance of coherent and incoherent beam configurations subjected to diffraction and thermal blooming effects. The propagation model also provides an additional damage assessment parameter—power-in-the-bucket—as well as the irradiance in the target plane for any laser wavelength. The propagation model results have target irradiance patterns similar to those obtained from WaveTrain, although the peak irradiance differs by ~30% due to differences in thermal blooming modeling. In addition, the propagation model can optimize certain beamlet configurations' peak irradiance using a genetic algorithm. Based on all the simulation results, a 13-beamlet configuration is deemed to have highest peak irradiance and power-in-the-bucket than all the tested multiple beam configurations.				
14. SUBJECT TERMS			15. NUMBER OF PAGES 101	16. PRICE CODE
17. SECURITY CLASSIFICATION OF REPORT Unclassified	18. SECURITY CLASSIFICATION OF THIS PAGE Unclassified	19. SECURITY CLASSIFICATION OF ABSTRACT Unclassified	20. LIMITATION OF ABSTRACT UU	

NSN 7540-01-280-5500

Standard Form 298 (Rev. 2-89)
Prescribed by ANSI Std. Z39-18

THIS PAGE INTENTIONALLY LEFT BLANK

Approved for public release. Distribution is unlimited.

**MODEL FOR ATMOSPHERIC PROPAGATION OF SPATIALLY COMBINED
LASER BEAMS**

Kum Leong Lee
Civilian, Defence Science Organisation National Laboratories
B.Eng., Nanyang Technological University, 2007

Submitted in partial fulfillment of the
requirements for the degree of

MASTER OF SCIENCE IN COMBAT SYSTEMS TECHNOLOGY

from the

**NAVAL POSTGRADUATE SCHOOL
September 2016**

Approved by: Joseph Blau
Thesis Co-Advisor

Keith Cohn
Thesis Co-Advisor

Kevin B. Smith
Chair, Department of Physics

THIS PAGE INTENTIONALLY LEFT BLANK

ABSTRACT

This thesis developed a propagation model that can be used to investigate the performance of coherent and incoherent beam configurations subjected to diffraction and thermal blooming effects. The propagation model also provides an additional damage assessment parameter—power-in-the-bucket—as well as the irradiance in the target plane for any laser wavelength. The propagation model results have target irradiance patterns similar to those obtained from WaveTrain, although the peak irradiance differs by $\sim 30\%$ due to differences in thermal blooming modeling. In addition, the propagation model can optimize certain beamlet configurations' peak irradiance using a genetic algorithm. Based on all the simulation results, a 13-beamlet configuration is deemed to have highest peak irradiance and power-in-the-bucket than all the tested multiple beam configurations.

THIS PAGE INTENTIONALLY LEFT BLANK

Table of Contents

1	Introduction	1
2	Overview of Directed Energy Weapons	3
2.1	History of DE	3
2.2	Advantages of DE Weapons	4
2.3	Disadvantages of DE Weapons	5
2.4	DE Source Technologies	5
2.4.1	Chemical Laser	5
2.4.2	Solid-State Laser	6
2.4.3	Free Electron Laser	7
3	Overview of Beam Combination Techniques	9
3.1	Incoherent Beam Combination	10
3.2	Coherent Beam Combination	14
3.2.1	Active Coherent Beam Combining	15
3.2.2	Passive Coherent Beam Combining	16
3.3	Spectral Beam Combination	19
4	Overview of Atmospheric Propagation	23
4.1	Atmospheric Absorption	23
4.2	Atmospheric Scattering	24
4.3	Atmospheric Turbulence	28
4.4	Thermal Blooming.	29
5	Simulation Methods	33
5.1	Diffraction Modeling	33
5.2	Thermal Blooming Modeling	37
5.3	Incoherent Beam Combining Modeling	39
5.4	Genetic Algorithm Modeling	39
5.5	Model Validation	43
5.5.1	Diffraction Model	44

5.5.2 Thermal Blooming Model.	45
6 Simulation Results	47
6.1 Diffraction Results.	50
6.1.1 Coherent Beam Combination	52
6.1.2 Incoherent Beam Combination	57
6.2 Thermal Blooming.	59
6.3 Genetic Algorithm.	69
7 Conclusions	73
7.1 Comparison with Analytical and WaveTrain Results	73
7.2 Beamlet configuration with constant irradiance	73
7.3 Beamlet configuration with varying irradiance.	74
7.4 Future Work	74
A.1 Appendix	75
List of References	77
Initial Distribution List	79

List of Figures

Figure 3.0.1	An example of tiled-aperture architecture (left) with individual laser beamlets represented by different colors and filled-aperture architecture (right) showing a single output beam.	10
Figure 3.1.1	Intensity of six beamlets at the output aperture. The X and Y axes, which represent the beamlets' position at the output aperture, are arbitrary units. The Z axis, which represents the intensity, is normalized to the beamlet's peak intensity at the output aperture.	11
Figure 3.1.2	Far-field pattern of a beam formed by incoherent beam combining (IBC). The X and Y axes, which represent the combined beam's position at far-field, are arbitrary units. The Z axis, which represents the intensity, is normalized to the beamlet's peak intensity at the output aperture.	12
Figure 3.1.3	Relationship of spot size w_o at the target and beam director radius $w(z)$	13
Figure 3.1.4	Beamlets bundled side by side at the beam director aperture is shown on the left and the actual beam director is shown on the right. . .	13
Figure 3.2.1	Beam formed by coherent beam combining (CBC) technique that uses tiled-aperture configuration. The X and Y axes, which represent the combined beam's position at far-field, are arbitrary units. The Z axis, which represents the intensity, is normalized to the beamlet's peak intensity at the output aperture.	14
Figure 3.2.2	Active CBC configuration using MOPA and electronic feedback.	15
Figure 3.2.3	Self-Fourier cavity.	19
Figure 3.3.1	SBC architecture developed by MIT Lincoln Laboratories and U.S. Air Force Research Laboratory.	20
Figure 4.2.1	Scattering probability(%) versus wavelength.	25
Figure 4.2.2	Aerosol absorption extinction coefficients for different wavelength generated using MODTRAN.	26

Figure 4.2.3	Aerosol scattering extinction coefficients for different wavelength generated using MODTRAN.	26
Figure 4.2.4	Molecular absorption extinction coefficient for different wavelength generated using MODTRAN.	27
Figure 4.2.5	Molecular scattering extinction coefficient for different wavelength generated using MODTRAN.	27
Figure 4.3.1	A laser beam propagating in a turbulent atmosphere in X-Z plane (left). The laser spot on the target plane (right). Both figures are from a wave propagation simulation. The color bar axis represents relative irradiance.	28
Figure 4.4.1	The laser irradiance pattern on the target due thermal blooming with $N_c = 1$. The color map represents the irradiance magnitude(i.e., dark red represents the highest intensity while light blue represents the lowest intensity).	32
Figure 5.1.1	Optical wave propagation coordinate system.	33
Figure 5.2.1	Method to obtain thermal blooming effects for laser propagating from source plane to target plane under the steady-state ($\frac{\partial \Delta T}{\partial t} = 0$) assumption.	37
Figure 5.2.2	Method to obtain thermal blooming effects for laser propagating from source plane to target plane under relaxed steady state condition.	39
Figure 5.4.1	An example of six equal radii beamlets enclosed in a one meter diameter beam director. The color map indicates the beamlet's intensity.	41
Figure 5.4.2	Another example of six beamlet configuration comprising of two different radii beamlets enclosed in a one meter diameter beam director. The color map indicates the beamlet's intensity.	42
Figure 5.4.3	The intensity variation of different radii beamlet configuration at a one meter diameter beam director output aperture. The color map indicates the beamlet's intensity.	42
Figure 6.0.1	The conduction loss directions are indicated by the blue arrows.	48

Figure 6.1.1	The irradiance pattern due to a 1kW single source at the beam director output aperture (left). The target irradiance pattern with a 10cm power-in-the-bucket circled in white (right). The color map represents the intensity.	51
Figure 6.1.2	The cross-sectional intensity plot at the target plane for $Y=0\text{cm}$ (left). Magnified view of the cross-sectional plot showing the first null point (right).	51
Figure 6.1.3	The cross-sectional intensity plot at the target plane for $X=0\text{cm}$ (left). Magnified view of the cross-sectional plot showing the first null point (right).	52
Figure 6.1.4	The irradiance pattern due to three coherent beamlets with 1kW output power at the beam director output aperture.	53
Figure 6.1.5	For the three coherent beamlets with 1kW output power, the target irradiance patterns for the propagation model (left) and Wave-Train (right). The 10cm diameter power-in-the-bucket is circled in white.	53
Figure 6.1.6	The cross-sectional intensity plot at the target plane for $X=0\text{cm}$ (left) as a result of the three coherent beamlets case. Magnified view of the cross-sectional plot showing the first null point (right).	54
Figure 6.1.7	The cross-sectional intensity plot at the target plane for $Y=0\text{cm}$ (left) as a result of the three coherent beamlets case. Magnified view of the cross-sectional plot showing the first null point (right).	54
Figure 6.1.8	The irradiance pattern due to 13 coherent beamlets of two different radii with 1kW output power at the beam director output aperture.	55
Figure 6.1.9	For the 13 coherent beamlets case with 1kW output power, the target irradiance patterns for the propagation model (left) and Wave-Train (right).	55
Figure 6.1.10	The cross-sectional intensity plot at the target plane for $X=0\text{cm}$ (left) as a result of the 13 coherent beamlets case. Magnified view of the cross-sectional plot showing the first null point (right).	56
Figure 6.1.11	The cross-sectional intensity plot at the target plane for $Y=0\text{cm}$ (left) as a result of the 13 coherent beamlets case. Magnified view of the cross-sectional plot showing the first null point (right).	56

Figure 6.1.12	The irradiance pattern due to 3 incoherent beamlets with 1kW output power at the beam director output aperture.	58
Figure 6.1.13	The irradiance pattern due to 13 incoherent beamlets of two different radii with 1kW output power at the beam director output aperture.	58
Figure 6.2.1	The irradiance pattern due to a single source with an output power of 1MW at the beam director output aperture. The color map indicates the intensity.	60
Figure 6.2.2	For the single beam case with 1MW output power, the target irradiance patterns for the propagation model (left) and WaveTrain (right).	60
Figure 6.2.3	The target irradiance patterns for the propagation model implementing transient thermal blooming.	61
Figure 6.2.4	The irradiance pattern due to three equal radii coherent beamlets with 1MW output power at the beam director output aperture.	62
Figure 6.2.5	For the three equal radii coherent beamlets case with 1MW output power, the target irradiance patterns for the propagation model (left) and WaveTrain (right).	63
Figure 6.2.6	A single beam at the beam director aperture with the same fill area and output power as the three equal radii, coherent beamlets configuration (left). The target irradiance pattern obtained using the propagation model (right).	63
Figure 6.2.7	The irradiance pattern due to six equal radii coherent beamlets with 1MW output power at the beam director output aperture (left). The target irradiance pattern with a 10cm power-in-the-bucket circled in white (right).	64
Figure 6.2.8	A single beam at the beam director aperture with the same fill area and output power as the six equal radii, coherent beamlets configuration (left). The target irradiance pattern obtained using the propagation model (right).	65
Figure 6.2.9	The irradiance pattern due to six coherent, different radii beamlets with 1MW output power at the beam director output aperture (left). The target irradiance pattern with a 10cm power-in-the-bucket circled in white (right).	66

Figure 6.2.10	A single beam at the beam director aperture with the same fill area and output power as the three beamlets configuration (left). The target irradiance pattern obtained using the propagation model (right). .	66
Figure 6.2.11	The irradiance pattern due to 13 coherent, different radii beamlets with 1MW output power at the beam director output aperture (left). The target irradiance pattern with a 10cm power-in-the-bucket circled in white (right).	68
Figure 6.2.12	The target irradiance pattern with a 10cm power-in-the-bucket circled in white obtained using WaveTrain.	68
Figure 6.2.13	A single beam at the beam director aperture with the same fill area and output power as the three beamlets configuration (left). The target irradiance pattern obtained using the propagation model (right). The color map indicates the intensity.	69
Figure 6.3.1	The irradiance pattern due to six coherent beamlets with two different radii and intensity at the beam director output aperture.	70
Figure 6.3.2	The irradiance pattern due to 13 coherent beamlets of two different radii and intensity with 1MW output power at the beam director output aperture.	71

THIS PAGE INTENTIONALLY LEFT BLANK

List of Tables

Table 4.1	Typical earth's atmosphere contents.	24
Table 5.1	Table illustrates how to pack beamlets of same radius optimally at the beam director output aperture.	40
Table 5.2	Parameters used during model validation.	43
Table 6.1	Target material made of aluminum.	49
Table 6.2	Beamlet configurations used for simulation.	50
Table 6.3	1kW coherent beamlet configuration results obtained using the propagation model.	57
Table 6.4	1kW incoherent beamlet configuration results obtained using propagation model.	59
Table A.1	Approximate Laser Power Level Needed to affect certain targets. .	75

THIS PAGE INTENTIONALLY LEFT BLANK

List of Acronyms and Abbreviations

ABL	Airborne Laser
ARPA	U.S. Advanced Research Projects Agency
CBC	coherent beam combining
DE	Directed Energy
DOD	Department of Defense
EO	Electro-Optical
FEL	Free Electron Laser
IBC	incoherent beam combining
INP	Innovative Naval Prototype
LaWS	Laser Weapon System
MIRACL	Mid-infrared Advance Chemical Laser
MOPA	master oscillator power amplifier
NPS	Naval Postgraduate School
SSL	Solid State Lasers
SBC	spectral beam combining
USAF	United States Air Force

THIS PAGE INTENTIONALLY LEFT BLANK

Acknowledgments

I would like to express my sincere gratitude to both my thesis advisors, Professor Keith Cohn and Professor Joe Blau, for sharing their knowledge, for their continuous support of my thesis, and for their endless patience.

I would also like to thank Dr. Conor Pogue, who assisted me in validating the propagation model by generating WaveTrain results for all my test cases.

I would also like to thank my wife, Amy, for supporting me throughout this journey and for being very attentive to our child's well-being. Without her endless sacrifices and encouragements, I would have never been able to fulfill my desire for continuous learning. I cherish and love you very much.

Finally, I would like to thank my organization, Defence Science Organisation National Laboratories, for awarding me a scholarship to attend the Master of Defence Technology and Systems programme, through which I attended two excellent institutions: the National University of Singapore and the Naval Postgraduate School. I hope that I can contribute to my organization with all the knowledge I gained.

THIS PAGE INTENTIONALLY LEFT BLANK

CHAPTER 1:

Introduction

Over the past several decades, the United States has researched and developed high-energy lasers for different platforms [1]. Although Directed Energy (DE) weapons are complex to design and costly, they deliver their payload at the speed of light [1]. However, the dwell time of a DE weapon imposes an engagement time constraint that reduces the DE weapon's capability of handling swarm and high-speed targets. Therefore, a short dwell time is desired for DE weapons during target engagement. An output of $\sim 1\text{MW}$ is required to kill many kinds of target in less than eight seconds based on an estimate developed in Chapter 6.

The entire thesis is based on Solid State Lasers (SSL) due to their deep magazine capability, relatively low cheap cost per kill, technological maturity and other factors to be discussed in Chapter 2. The current-state-of-the-art for a single solid-state laser source is only tens of kilowatts [2]. One approach to build a $\sim 1\text{MW}$ output power laser system is to spatially combine arrays of available high-power fiber lasers. In order to evaluate the performance of spatially combined laser beams, atmospheric modeling is essential as the laser beam propagates from the DE weapon through the atmosphere to the target.

Due to time constraints, the implementation of this propagation model only includes diffraction and thermal blooming effects for various laser beam configurations. In Chapter 2, the thesis starts with an overview of DE weapons and end with the different types of available laser sources. In Chapter 3, the thesis discussed various techniques to combine laser beams. In Chapter 4, the thesis discussed the atmospheric effects that a propagating laser beam would encounter. In Chapter 5, the thesis modeling tools is discussed. In Chapter 6, the thesis validated the model with analytical computations and simulations result from another propagation modeling tool, WaveTrain. In Chapter 7, the thesis discussed and concluded the performance differences between single source megawatt output lasers and those obtained using beam combination techniques during target engagement.

THIS PAGE INTENTIONALLY LEFT BLANK

CHAPTER 2:

Overview of Directed Energy Weapons

Unlike kinetic energy projectile weapons, DE weapons use high irradiance electromagnetic waves of a certain wavelength to inflict damage onto the intended target. The main damage mechanism from lasers is the ability to deposit huge thermal energy onto the target. The thermal energy deposited can result in melting, penetrating, and/or malfunctioning of the target's hardware. The actual degree of damage depends highly on the laser's power, dwell time, and beam quality. Table A.1 in the Appendix provides an estimate of the power level required to counter certain targets.

2.1 History of DE

In 1954, the Office of Naval Research funded Charles Townes to develop the laser. Charles Townes envisioned that lasers would be used as oscillators for optical communication. Gordon Gould proposed to the U.S. Advanced Research Projects Agency (ARPA) that a laser could be used to measure an enemy target's distance or act as a designator for missiles. He also concluded that a laser beam could be 10000 times brighter than the sun, an intensity that might "trigger chemical reactions or perhaps ultimately cause nuclear fusion" in nuclear missiles [3]. The first laser was developed by Theodore Maiman from Hughes Research Laboratories in 1960 [3]. The United States Air Force (USAF) awarded Maiman and various military labs contracts to develop lasers for missile guidance and communications. The first optical laser was based on a ruby gain medium and hence the output power was limited to tens of watts due to the ruby's material properties and lack of good thermal management. The Department of Defense (DOD) realized the potential of the laser as an operational military system from these inventions and invested heavily in its research and development. The Air Force Chief of Staff, General Curtis LeMay, commented on March 28, 1962, that "directed energy weapons would be able to transmit energy across space with the speed of light and bring about the technological disarmament of nuclear weapons." [3]. By mid-1965, C. Kumar N. Patel at Bell Labs developed a 200 W continuous wave gas laser. Subsequently, Hughes Research Laboratories developed a 1.5 kW with a 10 m oscillator

and a 54 m amplifier.

The key breakthrough for high-energy lasers came from addressing the heat transfer problem. Arthur Kantrowitz and Ed Gerry at the Avco Everett Research Laboratory near Boston addressed the laser's thermal issue by using a rocket-like approach: burning fuel to generate hot CO₂ and mixing with nitrogen before expanding through special nozzles at supersonic velocity [3]. The highly excited CO₂ molecules created the necessary population inversion conditions for lasing. In the 1970s, the USAF Airborne Laser laboratories developed the first aerial platform laser system, based on a 400 kW CO₂ laser. From the 1980s to the present, many laser systems such as the Mid-infrared Advance Chemical Laser (MIRACL), Airborne Laser (ABL), Laser Weapon System (LaWS), etc., have been successfully developed and tested. After the market appearance of the first commercial fiber laser in late 1980s, higher power single-mode fiber lasers have been continuously developed for machining. These high-power fiber lasers are potential sources for DE weapons due to their high wall plug efficiency. Finally, after decades of research and development on high-energy military lasers, DE weapons with the capability of countering certain targets at greater distances are ready to be installed in Navy ships.

2.2 Advantages of DE Weapons

The main advantage of DE weapons over kinetic weapons is their engagement speed and precision. Kinetic weapons require time for their projectiles to reach the target, and hence, engagement would be at closer range when compared to DE weapons, which engage at the speed of light. This fast engagement speed also gives DE an edge when handling rapidly maneuvering targets. In general, kinetic energy weapons cause collateral damage, unlike DE weapons, which allow the user to precisely select the aimpoint. The cost of target engagement for DE weapons is lower than that of tactical missiles as only electrical energy is required for laser operations. Although the initial setup costs for DE are high, the cost per shot and the other advantages mentioned make DE weapons a worthy long-term investment.

2.3 Disadvantages of DE Weapons

DE weapons require line-of-sight, and thus obscured targets cannot be engaged. Targets that are temporally obscured will increase the engagement time requirements. Due to these engagement time requirements, DE can only handle a limited amount of swarm targets, unlike kinetic energy weapons. Atmospheric conditions can also adversely affect DE weapons' range when compared to kinetic energy weapons.

2.4 DE Source Technologies

The source for DE weapons can be gas, chemical, solid state, or free electron lasers. Some of these laser sources have been successfully deployed by the United States. Gas technology was briefly covered in the history section. The following sections will focus on chemical, solid state, and free electron lasers.

2.4.1 Chemical Laser

Chemical lasers rely on chemical reactions for their pumping energy and more specifically, typically operate on molecular transitions, except in the case of atomic iodine. Chemical lasers produce near-to-mid infrared spectrum wavelengths. In these devices, mixed chemical vapors flow through the gain region in a direction that is transverse to the laser beam axis. Due to chemical reactions, toxic and combustible chemicals are produced, and hence residual gases must either be neutralized or collected for later disposal. The logistic handling of chemicals must also be considered in operational scenarios. To maximize the laser's efficiency, a special nozzle is used to control the flow conditions within the gain region. Although dealing with chemical lasers can be cumbersome, chemical lasers have been successfully tested for military applications. The U.S. Navy developed the first megawatt class laser known as the MIRACL, which was in operation from 1980 to 2000. MIRACL used the chemical deuterium fluoride to produce a 4 μm laser and was integrated with the SeaLite Beam director for operational testing. Due to MIRACL's wavelength, it was prone to absorption during atmospheric propagation. In the 1990s, the USAF developed another megawatt-class laser known as the ABL. The ABL used six chemical oxygen iodine 1.3 μm lasers within a modified Boeing 747 airplane. In 2010 field testing, the ABL successfully

intercepted and destroyed ballistic missiles during their initial boost phase [1]. However, the program was discontinued due to economic and practical issues.

2.4.2 Solid-State Laser

Certain materials that consist of crystals or glass with specific atomic ions imbedded are excellent for the laser gain medium. The specific atomic ions must have a long radiative decay lifetime and favorable absorption band, allowing pumping light to be effectively absorbed. SSLs use optical pumping to create population inversion conditions for lasing. The optical pumping can be provided by another laser, a semiconductor diode, or a flashlamp. There are various types of SSL structures but only fiber and slab SSLs have been used as DE weapons.

2.4.2.1 Slab Solid-State Lasers

In a slab SSL, the gain medium is a large plate-like structure. The DOD's Joint High Power SSL (JHPSSL) program developed a DE prototype known as the Maritime Laser Demonstration (MLD) that leveraged slab SSL technology. In 2010, the MLD project group coherently combined seven 15 kW slab SSLs to create a 1.064 μm laser with an output power of 105 kW [1]. During field testing, the MLD successfully tracked and engaged small boats in a marine environment. In May 2011, a Northrop representative stated that they "could build the first unit of a full-power engineering and manufacturing development (EMD) version of the MLD within four years, if the Navy could find the resources to fund the effort" [1]. However, given the current-state-of-the-art, slab SSLs cannot be scaled to megawatt power levels as the slab is not readily cooled due to low surface to volume ratio [1].

2.4.2.2 Fiber SSL

In a fiber SSL, the gain medium is a flexible fiber cable that is more readily cooled than a slab, due to an improved surface to volume ratio. A fiber SSL consist of a laser diode pump, a wavelength-selective coupler that allows the pump wavelength to enter the fiber gain medium without disturbing the signal, an amplifier spliced into the fiber gain medium,

and an optical isolator. High power fiber lasers are widely used in material cutting and for DE weapons. One of the most prominent full operational fiber lasers system is the Laser Weapon Systems (LaWS), which has been deployed on the USS *Ponce* since 2014.

2.4.2.3 LaWS

The LaWS project started in 2010 [4] and was awarded to Kratos Defense and Security solutions by the Naval Surface Warfare Center. LaWS was designed to be integrated with the existing Phalanx Close-In-Weapon System (CIWS) with the intent to disable/jam Electro-Optical (EO) sensor suites and to counter UAVs/ EO guided bombs with the assistance of radar. LaWS combined six 5.5kW IPG Photonics fiber lasers to produce a total output power of 33 kW with a beam quality of 17 [1]. The wavelength of each fiber laser is $1.06\ \mu\text{m}$ and is near an atmospheric transmission window ($1.045\ \mu\text{m}$). To ensure LaWS effectiveness, it was tested with different intended targets under various combat scenarios. In June 2009, LaWS accurately engaged five UAVs at China Lake in southern California [1]. In May 2010, LaWS accurately engaged four UAVs at 1 nautical mile away from San Nicholas Island [1]. During the same tests, LaWS also demonstrated the ability to destroy rigid-hull inflatable boat materials at about half a nautical mile and also disabled EO/infrared sensors. Between July and September 2012, LaWS accurately engaged three UAVs when the system was on an Arleigh Burke class destroyer. LaWS was installed on the USS *Ponce* for a one year trial as of August 2014 and was declared as an operational asset in September 2014 [1]. If all the testing goes well, the U.S. Navy could deploy laser weapons operationally in the near future.

2.4.3 Free Electron Laser

A Free Electron Laser (FEL) consists of free electrons in vacuum as the gain medium, a radio-frequency linear accelerator (linac) as the pumping source, alternating magnetic field as an undulator, laser resonator mirrors, and an output coupler [5]. Unlike conventional lasers that rely on population inversion in a gas or solid-state material, a FEL uses relativistic electrons from a linac, which pass through an undulator, causing them to oscillate and therefore produce light. During these oscillations, the electrons radiate in a relativistic dipole radiation pattern that maximizes in a direction perpendicular to the oscillation direction. The

electrons' relativistic speed causes the oscillation frequency to shift from a lower frequency in their rest frame to a higher frequency in the laboratory frame. The radiation frequency depends on the electrons' kinetic energy and the period of the alternating magnetic field. Mirrors are placed at opposite ends of the laser cavity to reflect a portion of the radiated energy back through the alternating magnetic fields. The reflected light stimulates additional radiation that produces a strong optical beam within and beyond the laser cavity. Existing FELs have wavelength ranges from 0.06 nm to 3 mm [6] with scalable output power up to 1 GW for pulsed lasing and 10 W for continuous lasing. The current-state-of-the-art for high average power FELs is 14 kW at Jefferson National lab. The FEL's wavelength can be tuned for optimal atmospheric transmission and has excellent beam quality suitable for DE applications. FEL technology is thought to be scalable to MW class since there is no conventional substrate to damage. The energy of spent electrons can be recovered to increase wall plug efficiency. Currently, FELs tend to be large (~20 m), heavy, and expensive. During FEL operation, additional radiation shielding is required due to Bremsstrahlung radiation produced by the electrons. Around 2010, the U.S. Navy had a plan known as Innovative Naval Prototype (INP) to develop a ~100kW class FEL, but the INP was shelved in ~ 2012 due to the immaturity of FEL technology, and the technology advancement in fiber laser. the U.S. Navy may eventually reassess FEL technology to achieve ~MW power level single laser source system.

CHAPTER 3:

Overview of Beam Combination Techniques

A weapon's effectiveness on the battlefield can be measured using the probability of damage. Fragmentation and blast warheads increase the probability of damage by ensuring sufficient coverage area. For DE weapons, the probability of damage depends on beam power, beam quality, dwell time, slant range, weather, atmospheric conditions, etc. The beam power refers to the total amount of power contained within the laser beam as it exits the DE weapon. The beam quality parameter characterizes its focusability, which affects the laser's irradiance and spot size on the target's surface. Dwell time refers to the time required for the laser to damage the target.

For DE weapons to be considered lethal for many applications, they need to destroy targets within seconds of engagement and thus they require a laser beam power from hundreds of kilowatts to megawatts with good beam quality; the actual output power needed depends on the target and the atmospheric conditions, and the laser system itself. The continuous advancement of laser technologies might eventually lead to the development of a single laser source that has hundreds of kilowatts or even megawatts of output power. Current solid-state lasers are largely limited by thermo-optic or other non-linear effects that set a limit on the output power. Although fiber lasers have large surface to volume cooling area, they are still vulnerable to thermally induced damage above a threshold power. A single mode fiber laser's output power will saturate at several kilowatts unless there is a major breakthrough in the fiber's mode control and better thermal solutions [2]. An alternative approach to building high-power laser systems is to combine arrays of commercially available high power fibers. Over the past several decades, researchers have advanced the state of laser beam combination technology. Currently, it is possible to design a laser system with tens of kilowatts of output power and good beam quality using an array of laser beams.

Beam combining techniques for laser arrays can be characterized in three broad classes: incoherent, coherent, and spectral beam combining. These combination techniques can have either a tiled-aperture or a filled-aperture architecture. The tiled-aperture architecture has several laser beams aligned with optics, allowing them to be bundled at the output aperture of a DE weapon, whereas the filled-aperture architecture has these several beams

overlaid to cover the entire beam director mirror, as illustrated in Figure 3.0.1. To compare beam combination techniques, one could consider the laser’s irradiance on the target or the power in the bucket.

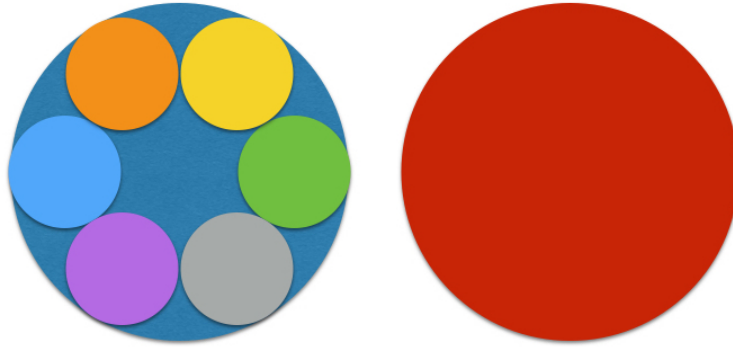


Figure 3.0.1: An example of tiled-aperture architecture (left) with individual laser beamlets represented by different colors and filled-aperture architecture (right) showing a single output beam.

3.1 Incoherent Beam Combination

The working principle of the incoherent beam combining (IBC) technique is to focus all the beamlets onto the target without accounting for their individual phases. The IBC technique can be implemented using either a filled-aperture or a tiled-aperture architecture. For the filled-aperture architecture, the laser beamlets are combined in a fiber that degrades the beam quality significantly and thus is not suitable for DE weapons. For the tiled-aperture architecture shown on the left in Figure 3.0.1, the laser beamlets are bundled side-by-side. The beamlets may or may not have the same wavelength; even those with the same wavelength may have random wavefront phase or polarization relative to one other. The beamlets must be aligned so that they will overlap at the same spot on the target. The total irradiance produced by IBC will be N times the individual beamlet irradiance where N is the number of beamlets, and the overall combined beam waist diameter is inversely proportional to each beamlet’s diameter. Figure 3.1.1 shows the intensity pattern of six beamlets at the beam director’s output aperture. Figure 3.1.2 shows the far-field pattern of a beam formed by the IBC technique after the six beamlets propagate through the atmosphere [7]. Figure 3.0.1

and Figure 3.1.1 do not have any central beamlet as the beam director's secondary mirror occupies that position as shown on the right in Figure 3.1.4.

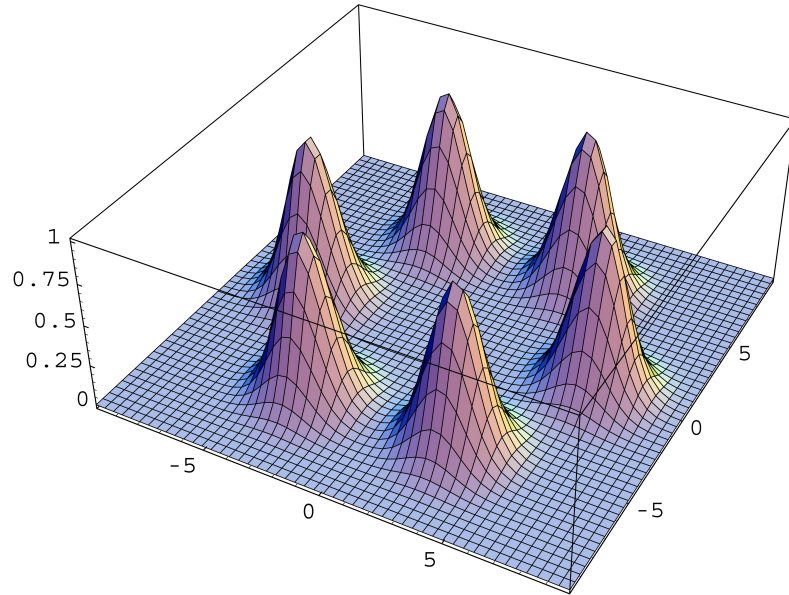


Figure 3.1.1: Intensity of six beamlets at the output aperture [7]. The X and Y axes, which represent the beamlets' position at the output aperture, are arbitrary units. The Z axis, which represents the intensity, is normalized to the beamlet's peak intensity at the output aperture.

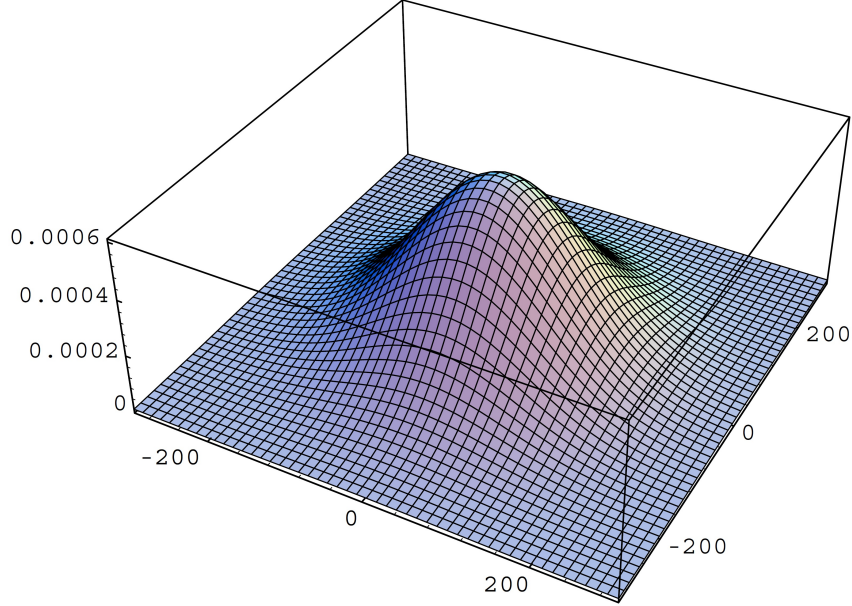


Figure 3.1.2: Far-field pattern of a beam formed by IBC [7]. The X and Y axes, which represent the combined beam's position at far-field, are arbitrary units. The Z axis, which represents the intensity, is normalized to the beamlet's peak intensity at the output aperture.

The IBC technique has numerous advantages over coherent and spectral combining. This approach does not require the individual beamlets to have narrow line widths or to have the same phase or polarization. Without considering the atmospheric turbulence effects, the spot size of a Gaussian laser beam propagating in free space is given as

$$w(z) = w_o \left(1 + \left(\frac{z}{Z_R} \right)^2 \right)^{1/2}, \quad (3.1)$$

where $Z_R = \pi w_o^2 / \lambda$ is the Rayleigh length and w_o is the spot size at the focus, as shown in Figure 3.1.3.

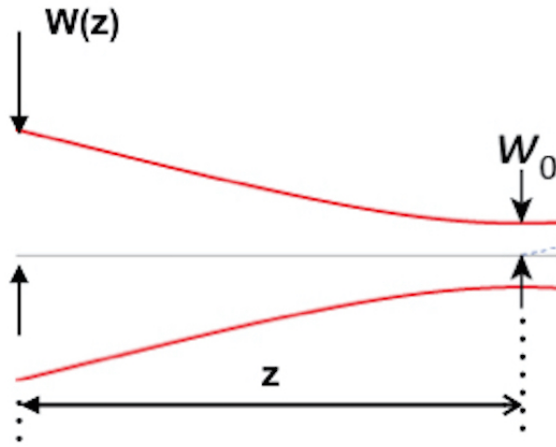


Figure 3.1.3: Relationship of spot size w_o at the target and beam director radius $w(z)$.

To obtain a small spot size and thus high irradiance on the target, each beamlet must have good optical beam quality, and its diameter must be sufficiently large at the output aperture. According to Equation 3.1, a small w_o spot will result in shorter Rayleigh length. Therefore, the system requires multiple large beam expanders or telescopes. In theory, IBC laser systems can be scalable to any power level required for DE applications, but the beam director radius is a function of each beamlet diameter(a), $R_{BeamDir} \approx N^{1/2}a$, as shown in Figure 3.1.4 [8].

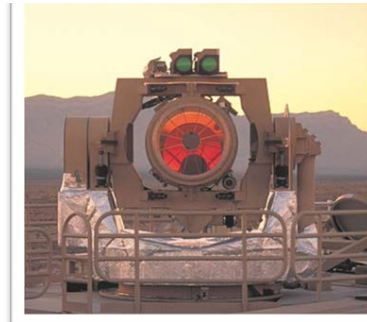
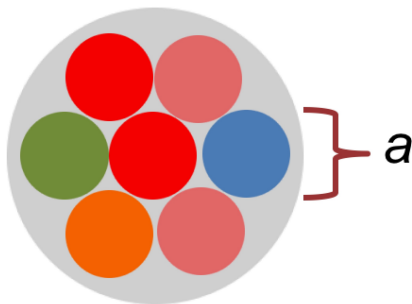


Figure 3.1.4: Beamlets bundled side by side at the beam director aperture is shown on the left and the actual beam director is shown on the right.

3.2 Coherent Beam Combination

The working principle of the coherent beam combining (CBC) technique is to get all the beamlet's individual phases to be the same by using phase correction mechanisms. The total irradiance produced by CBC will be N^2 times the individual beam irradiance, and the overall combined beam waist diameter is approximately inversely proportional to the overall diameter of the array. Figure 3.2.1 shows the far-field pattern of a beam formed by the CBC technique from six beamlets at the beam director's output aperture as shown in Figure 3.1.1. Figure 3.2.1 also shows side lobes that are formed by constructive interference of the individual beamlets [7].

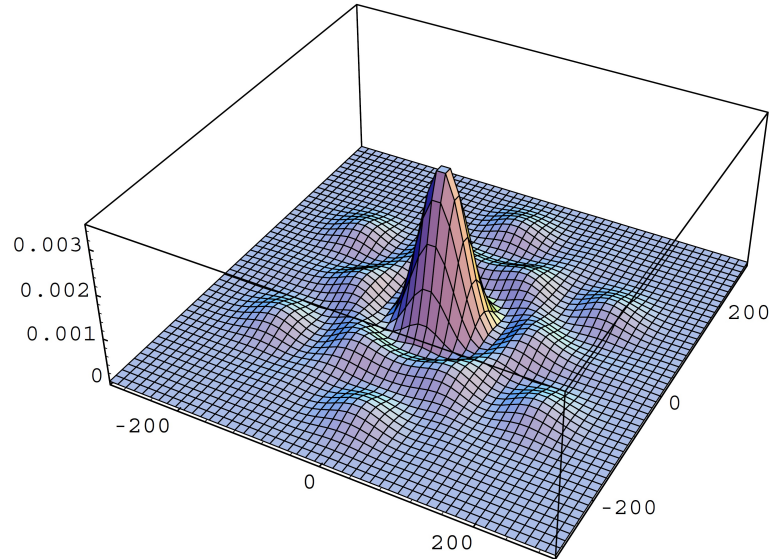


Figure 3.2.1: Beam formed by CBC technique that uses tiled-aperture configuration [7]. The X and Y axes, which represent the combined beam's position at far-field, are arbitrary units. The Z axis, which represents the intensity, is normalized to the beamlet's peak intensity at the output aperture.

The CBC technique is subdivided into active and passive techniques.

3.2.1 Active Coherent Beam Combining

Active coherent beam combining techniques can have either a filled-aperture or tiled-aperture architecture. For the tiled-aperture architecture, a master oscillator power amplifier (MOPA) and electronic phase feedback system are used to alter the individual laser beamlets' phases as shown in Figure 3.2.2.

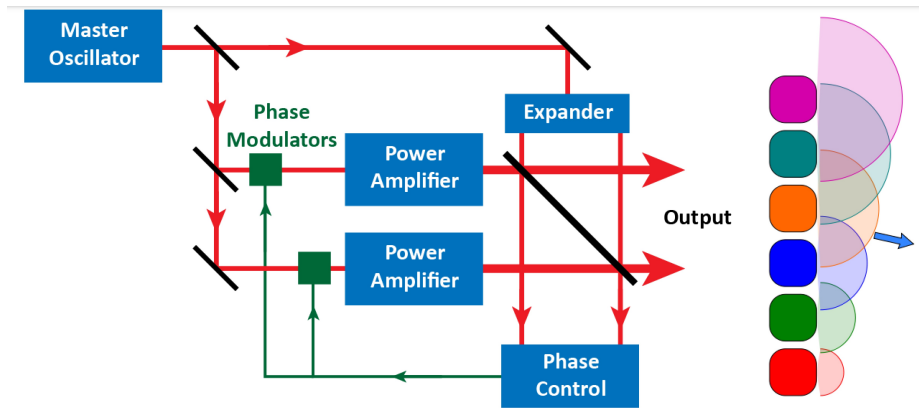


Figure 3.2.2: Active CBC configuration using MOPA and electronic feedback.

To provide a coherent input to each individual laser's amplifier, the MOPA output must be polarized with a narrow line width spectrum. The electronic phase feedback system can actively adjust each individual beamlet's phase to compensate for any phase differences between the beamlets.

The phase feedback system can also be used as a small angle beam steerer to assist aiming by varying the beamlet phases to change the constructive interference pattern on the target. This change in aiming would be due to changes in the combined beam's wavefront. This beam steering method is similar to the working principles of active phased array antennas in radar.

The fiber length differences between the beamlets are very crucial for the computation of the phase feedback, which is the input for the path length adjusters. Since the phase of beamlets can be adjusted, it is possible to compensate for low atmospheric turbulence.

Any active CBC that uses a tiled-aperture configuration would introduce side lobes that

would decrease the maximum peak irradiance on the target if there are gaps within the beamlets, as shown in Figure 3.2.1. In addition, variation between the individual amplitudes of the beamlets could increase these side lobes.

The tiled-aperture CBC technique cannot achieve more than 75% irradiance when compared with a perfect Gaussian beam due to its side lobes [8]. For the coherent tiled aperture beam combiner, the larger separation between the beamlets and the non-uniform illuminated subapertures reduce the amount of irradiance on the target. A waveguide combiner can theoretically be used to compensate for the irradiance drop. In a square or rectangular waveguide, an input beam reproduces itself after travelling for a distance known as the Talbot length given by

$$L_T = \frac{4nh^2}{\lambda}, \quad (3.2)$$

where n is the refractive index inside the waveguide, and h is the internal dimension of the waveguide. If the waveguide terminates before the Talbot length, these beams are separated into multiple beams that are then coherently combined into a single output beam. If a larger separation between the entry beams is desired, a tapered waveguide must be designed. Lockheed Martin Corporation has been conducting waveguide coherent combining experiments for a tiled-aperture architecture [8]. Northrop Grumman Corporation researchers have also used another method, involving a diffractive optical element rather than a waveguide, to produce high beam quality beams for a coherently combined tiled-aperture architecture [8]. Although the fill-factor of the output aperture has increased, the electronic steering and automatic aberration ability of the beams have decreased.

3.2.2 Passive Coherent Beam Combining

The passive CBC techniques use optical feedback from the fibers to lock all the beamlets' phases. Current examples are the fiber ring and the self-Fourier cavity. Unlike the active CBC technique, the passive CBC techniques do not require narrow line width output. This allows a single fiber to operate at a higher output since the onset of damaging nonlinear effects is delayed for broader spectrum beams. However, there are still technical issues associated with the scalability of the passive CBC techniques, and hence this thesis will not focus on them.

3.2.2.1 Fiber Ring

This technique uses a spatial filter, which includes a focusing lens and pinhole, to select those longitudinal modes that interfere with constructive laser combination. Fiber lasers have many longitudinal modes due to their length and large line width, and hence the probability of finding the appropriate longitudinal mode for constructive interference is higher. The fiber ring CBC technique can be mathematically described by [8]

$$E = \sum_{j=1}^K A_j e^{-i \frac{2\pi}{\lambda_j} n L_j} , \quad (3.3)$$

where K is the number of fibers used, n is the fiber core refractive index, A_j is the mode amplitude, and L_j is the length of j^{th} fiber. The feedback signals to the fiber amplifiers are proportional to $|E^2|$ and are maximized when the wavelengths are

$$\frac{n L_j}{\lambda_j} = m_j , \quad (3.4)$$

where m_j is an integer. Currently, Northrop Grumman Information Technology Sector researchers have successfully combined 16 fibers using this technique [8]. The passive ring CBC technique produces good laser beam quality and is relatively simple as it does not require any phase locking system or polarization-maintaining fiber. Since it can automatically select any of the longitudinal modes, it can compensate for any thermal and mechanical perturbation. This technique enables higher output power scalability since it can operate with broadband fibers, which are inexpensive. However, this technique requires a lens that might distort the wavefront due to the high heat load imparted from the high-power sources.

3.2.2.2 Self-Fourier Cavity

Unlike the Fiber Ring CBC technique, the Self-Fourier technique relies on a Fourier lens to spatially separate the beamlets before reflecting them back to the input sources for coherent combination. All these inputs sources, which reside in the input plane one focal length away from the Fourier lens, are pointing along the optical axis and hence are centered on the optic axis in the Fourier plane, which is one focal length beyond the lens.

Consider a beamlet located at a distance d_1 away from the optical axis. After passing through the Fourier lens, it is collimated with a propagation angle given by

$$\theta = \frac{d_1}{F} \ll \pi, \quad (3.5)$$

where F is the focal length of the Fourier lens. Due to the small propagation angle, the phase along the Fourier plane is

$$\phi = kx \sin(\theta) \cong kx \frac{d_1}{F}, \quad (3.6)$$

where k is the wavenumber, and x is the distance from the optical axis. If x is a multiple of

$$d_2 = \frac{\lambda F}{d_1}, \quad (3.7)$$

the phase will be a multiple of 2π and will constructively interfere in the Fourier plane with patterns d_2 apart. If d_2 is equal to d_1 , then

$$d_1 = \sqrt{\lambda F}, \quad (3.8)$$

and the interference pattern at the Fourier plane will be similar to the original pattern of sources at the input plane.

If the Fourier plane is configured to coincide with the input plane, which can be implemented by cutting the Fourier lens in half and adding a partially reflective mirror, the feedback pattern will theoretically be coupled back to the input sources when the beams are coherent, as shown in Figure 3.2.3. As the beamlet's power increases, temperature variation across the surface of the lens and mirror may exist as cooling can only occur at their edges to prevent interfering with the optical path. This temperature variation will affect the geometric characteristic of the lens and thus resulting in beam distortion.

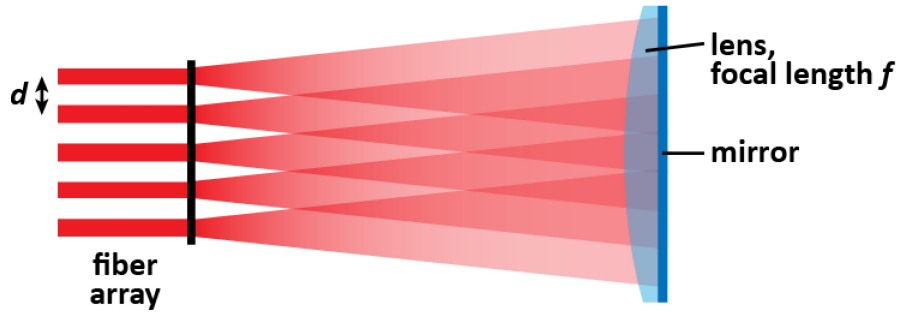


Figure 3.2.3: Self-Fourier cavity.

3.3 Spectral Beam Combination

The spectral beam combining (SBC) technique uses a dispersive optical element, such as a diffraction grating or prism, to spatially combine beams of different wavelength. This technique is similar to the wavelength-division multiplexing technique used in optical communications. The SBC technique requires each beam's direction and wavelength to be controlled. The implementation of the SBC technique is easier than CBC as controlling wavelength is simpler than phase. Laser resonators that are combined using the SBC technique share the same output mirror. These beams are parallel and are focused at the desired range. For a particular laser element, the incident angle that the beam hits the dispersive optical element determines the oscillating frequency in the case where the grating element is part of the cavity. The bandwidth of the laser gain mediums must be able to support all these oscillation frequencies.

Together with the U.S. Air Force Research Laboratory, MIT Lincoln Laboratories developed a SBC architecture that uses a lens to focus the parallel laser inputs [9]. Each of these inputs is separated by distance X_j and then focused by the lens on the dispersive optical element, as shown in Figure 3.3.1.

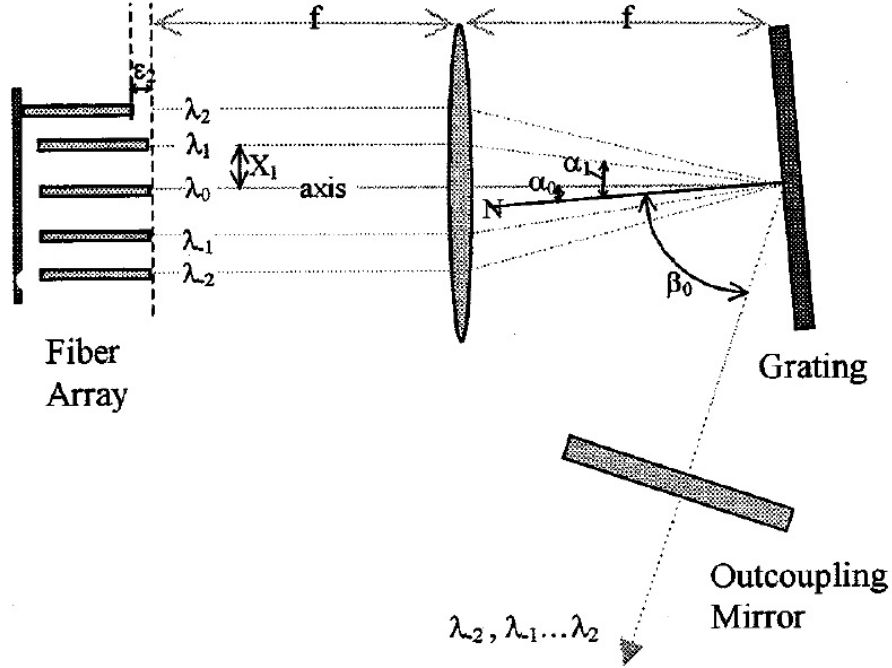


Figure 3.3.1: SBC architecture developed by MIT Lincoln Laboratories and U.S. Air Force Research Laboratory. Source: [9].

The diffraction angle caused by the grating material depends on the incoming beam's wavelength. An incident plane wave with wavelength λ propagating in the direction orthogonal to the grating grooves will be diffracted according to [9],

$$\sin(\beta) - \sin(\alpha) = \frac{m\lambda}{l}, \quad (3.9)$$

where m is the diffraction order; α and β are the incident angle and reflected angle of the wave, respectively, at the grating surface; and l is the grating period. Taking the derivative of equation 3.9 with respect to incident angle α will result in

$$\frac{\Delta\lambda}{\Delta\alpha} = -\frac{l \cos(\alpha)}{m}. \quad (3.10)$$

The fiber separation is approximately

$$X_j \cong \Delta\alpha \times f, \quad (3.11)$$

where f is the focal length. Substituting $\Delta\alpha$ from equation 3.10 into equation 3.11,

$$\Delta\lambda \cong -\frac{lX_j \cos(\alpha)}{mf}. \quad (3.12)$$

From equation 3.12, the spatial separation of the fibers determines the difference in each fiber's operating wavelength, and hence the wavelength will not be evenly distributed for constant fiber spacing because of the $\cos(\alpha)$ term. In addition, the diffracted beam will have an angular spread that is larger than that of the incident beam due to each fiber's finite line width. The divergence angle deviation is given by

$$\Delta\theta \cong \frac{\Delta\lambda^* m}{l \cos(\beta)}, \quad (3.13)$$

where $\Delta\lambda^*$ is the bandwidth of an individual fiber. Due to this additional angular spread, the beam quality, M^2 , becomes worse as compared to a single fiber laser source.

$$M^2 \cong \sqrt{1 + \left(\frac{\Delta\lambda^* m \pi \omega_o}{2l \lambda \cos(\beta)} \right)^2}, \quad (3.14)$$

where ω_o is the beam waist. The power scaling of SBC is limited by the grating's thermal capacity, fiber gain bandwidth, and power limits for fibers with narrow linewidth. To illustrate the beam quality obtainable using the SBC technique, consider a source comprised of Gaussian beams with wavelength of $\lambda = 1\mu\text{m}$. The source's beam waist is assumed to be $\omega_o = 1.5\text{ cm}$ with $\Delta\lambda^* = 1 \times 10^{-9}\text{m}$ and the grating's blaze spacing, l , is assumed to be $1\mu\text{m}$. Using these assumptions, $M^2 \cong 23.6$ according to equation 3.14 when $\cos\beta = 1$.

THIS PAGE INTENTIONALLY LEFT BLANK

CHAPTER 4:

Overview of Atmospheric Propagation

The Earth's atmosphere contains many different constituents that vary based on location and time. The presence of these constituents introduces atmospheric absorption and scattering effects that reduce a DE weapon's effectiveness by attenuating the optical beam energy. In addition, the density and temperature of the Earth's atmosphere both fluctuate and thus can introduce turbulence, further reducing a DE weapon's effectiveness. Because a DE weapon's laser wavelength is typically in the infrared region, this chapter will only focus on the atmospheric effects that impact these wavelengths.

4.1 Atmospheric Absorption

The atmosphere's constituents can be classified into two main categories: molecules and aerosols. As shown in Table 4.1, the Earth's atmosphere is mainly comprised of nitrogen, oxygen, argon, carbon dioxide, and water vapor. The nitrogen and oxygen molecules are linear, homonuclear diatomic molecules that have symmetrical bonds. Due to these symmetrical bonds, their dipole moments will not absorb any propagating laser beam that is in the infrared spectrum. Unlike the nitrogen and oxygen molecules, the remaining molecules have asymmetrical bonds causing their dipole moments to absorb radiation in certain parts of the infrared spectrum. Thus, maximum energy can only be deposited on the target if the laser beam's wavelengths are not within the absorption regions of these molecules. The aerosol absorption effects on propagating laser beams are similar to the molecular effects, but these effects depend substantially on the aerosols' size and content.

Content	Composition
Nitrogen	78%
Oxygen	21%
Argon	0.9%
Carbon dioxide	0.03%
Water Vapor	0-4%

Table 4.1: Typical earth's atmosphere contents. Adapted from [10].

4.2 Atmospheric Scattering

Additionally, laser beams are often scattered during propagation by molecules and suspended aerosols in the Earth's atmosphere. The nature of these scattering effects depends on the optical beam's wavelength and the size of the scattering agents. For wavelengths that are smaller than $\sim 5 \mu\text{m}$, the probability of scattering an optical beam is inversely proportional to the fourth power of the optical beam's wavelength. This type of scattering, known as Rayleigh scattering, occurs when the scatterer is much smaller than the wavelength. The nitrogen and oxygen molecules in the Earth's atmosphere are the primary causes of this Rayleigh scattering. For example, the shorter wavelengths from the sun are scattered by the Earth's atmosphere, which is why the sky appears blue during the day. The deflection of photons tends to be random Rayleigh scattering. As the size of the scattering agent increases, full Mie scattering occurs. Mie scattering is more directional than Rayleigh scattering as it increases in the forward direction. The most common Mie scattering agents in the Earth's atmosphere are fog, smoke, and dust particles. Mie scattering plays an important role in laser beam propagation since these beams are in the infrared spectrum. When the scattering agents' size becomes ten times larger than the optical beam's wavelength, non-selective scattering occurs. Mist and fog appear to be white due to Mie scattering effects. Figure 4.2.1 shows the three scattering processes [11].

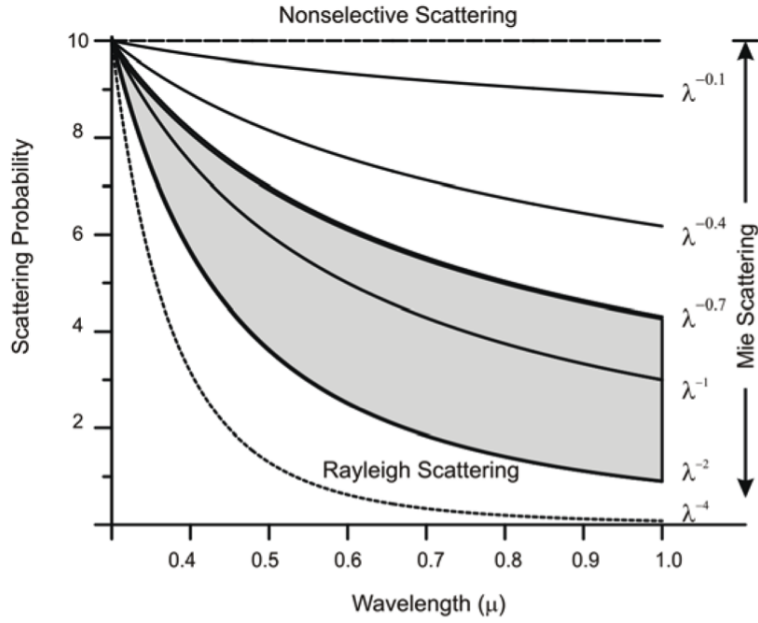


Figure 4.2.1: Scattering probability(%) versus wavelength.
Adapted from [11].

The combined effects from absorption and scattering for an optical beam propagating through a linear medium can be modeled by Beer's law,

$$P(z) = P_o e^{-\epsilon z} , \quad (4.1)$$

where $P(z)$ represents the power of the optical beam at z distance away from the source and P_o is the output laser power from the DE weapon. The variable ϵ is known as the extinction coefficient, given by

$$\epsilon = \alpha_m + \alpha_a + \beta_m + \beta_a , \quad (4.2)$$

where α and β represent absorption and scattering coefficients, respectively, and subscripts a and m represent molecular and aerosols contributions, respectively. Figure 4.2.2, 4.2.3, 4.2.4, 4.3.1 illustrate the absorption and scattering coefficient due to molecular and aerosols.

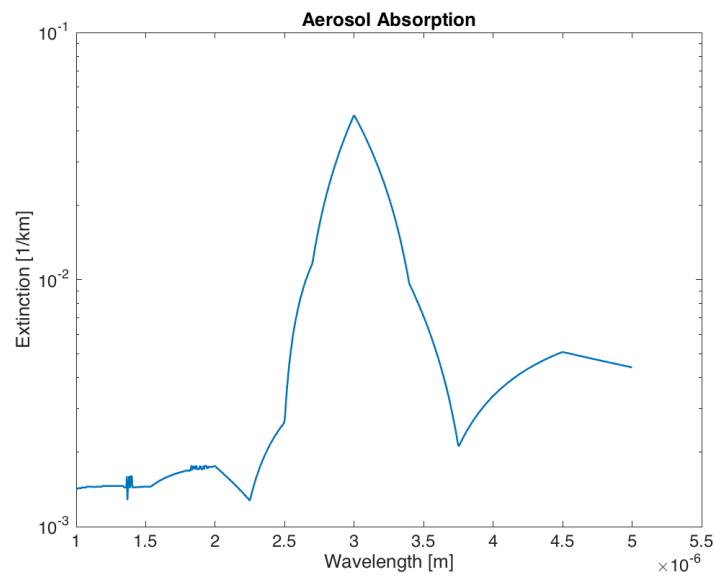


Figure 4.2.2: Aerosol absorption extinction coefficients for different wavelength generated using MODTRAN.

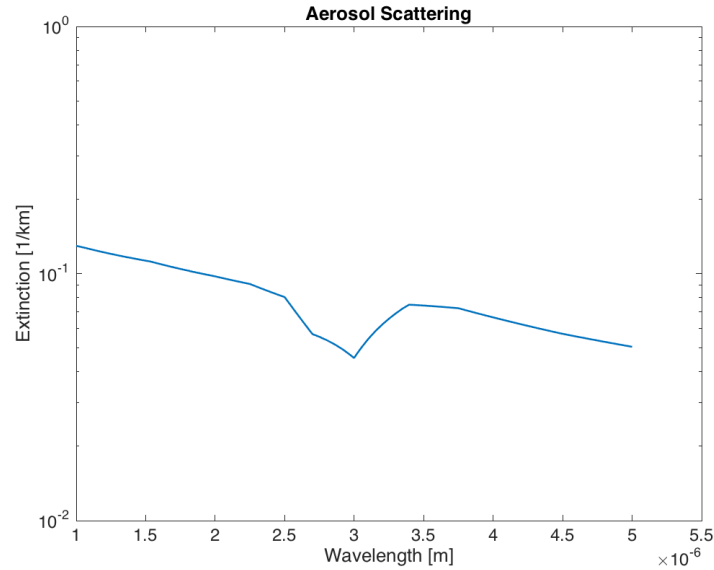


Figure 4.2.3: Aerosol scattering extinction coefficients for different wavelength generated using MODTRAN.

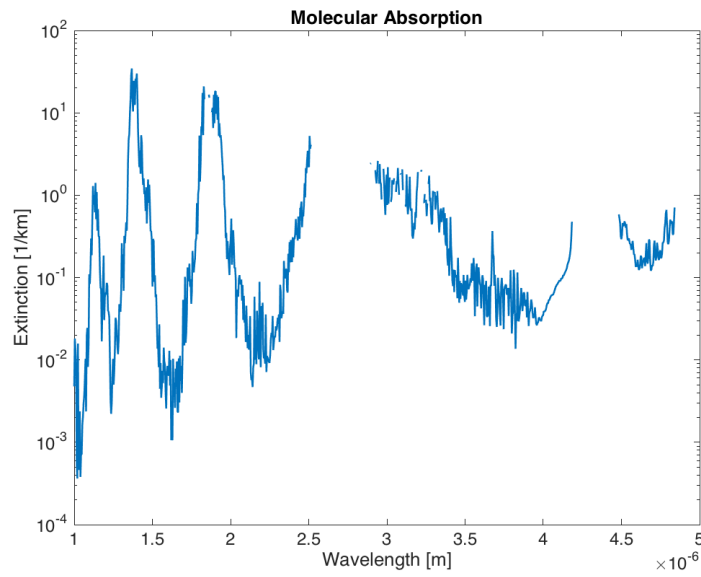


Figure 4.2.4: Molecular absorption extinction coefficient for different wavelength generated using MODTRAN.

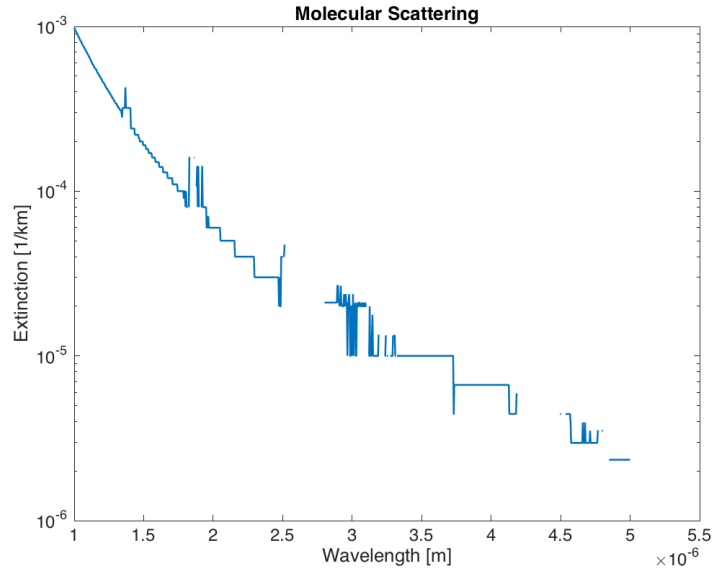


Figure 4.2.5: Molecular scattering extinction coefficient for different wavelength generated using MODTRAN.

4.3 Atmospheric Turbulence

Fluctuations in the density and temperature of the Earth's atmosphere can cause the air's index of refraction to vary, thus changing the beam's propagation pattern, affecting the direction and focus of the beam. The index's variation due to temperature, wavelength, and pressure can be modeled as [12]

$$n \approx 1 + 77.6 \times 10^{-6} [1 + 7.52 \times 10^{-3} \lambda^{-2}] \frac{P}{T}, \quad (4.3)$$

where n is the refractive index, λ is the optical beam wavelength in μm , P is the pressure in mbar, and T is absolute temperature in Kelvins.

Due to this variation, the propagating laser beam can spread, affecting the aim point as shown in Figure 4.3.1. The intended laser spot on the target in Figure 4.3.1 is in the center, but the final spot location is different due to the effect of turbulence.

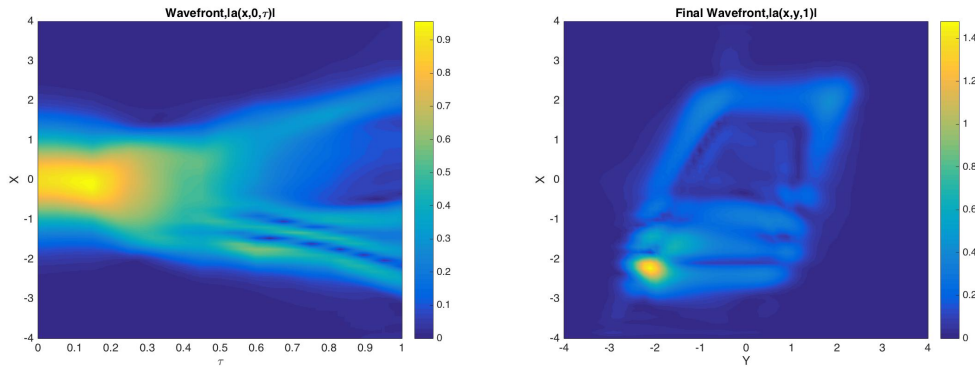


Figure 4.3.1: A laser beam propagating in a turbulent atmosphere in X-Z plane (left). The laser spot on the target plane (right). Both figures are from a wave propagation simulation. The color bar axis represents relative irradiance.

Turbulence development is a nonlinear process that can be described by the Navier-Stokes equations. However, the solutions to the Navier-Stokes equation are unstable for finite perturbations at large Reynolds numbers. Instead, Kolmogorov's theory based on a statistical method is used to predict turbulence using the C_n^2 value [13]. The C_n^2 value represents the

amount of turbulence in the atmosphere that the beam is propagating through. Strong turbulence exhibits a C_n^2 value of $10^{-13} m^{-2/3}$ or more, while a typical weak turbulence exhibits a C_n^2 value of $10^{-17} m^{-2/3}$ or less. Due to less influence of surface heating, the C_n^2 value at higher altitudes tends to decrease.

The Fried parameter, r_o , measures how well the laser beam can maintain coherence through the atmosphere that has varying refractive index. For a spherical wave, the r_o parameter is given by

$$r_o \approx 0.33 \frac{\lambda^{\frac{6}{5}}}{(l C_n^2)^{\frac{3}{5}}}, \quad (4.4)$$

where l is the distance from the target. When turbulence is sufficiently strong, r_o is used to determine the target spot size (Equation illustrated in Chapter 3) instead of the beam director diameter.

4.4 Thermal Blooming

As the high-power laser propagates through the atmosphere, some parts of its energy are absorbed by molecules and aerosols. This absorption process causes the air to have temperature gradients that ultimately change the air's density. The heated air expands out radially, decreasing the air's density and hence reducing the index of refraction. This reduction in the index of refraction, modeled by Equation 4.3, is equivalent to placing a diverging lens along the beam's propagation path, reducing the beam's peak irradiance on the target. This effect is known as thermal blooming.

Before deriving the thermal blooming equations, the beam propagation must first be analyzed using the paraxial wave equation [14],

$$\frac{\partial \psi}{\partial z} = -\frac{\epsilon}{2} \psi + \frac{i}{2k} \nabla_{\perp}^2 \psi + (ik \delta n) \psi, \quad (4.5)$$

where ϵ is the extinction coefficient in Equation 4.2; $i/2k \nabla_{\perp}^2 \psi$ represents the beam's transverse diffraction; and $(ik \delta n) \psi$ describes the effects of the refraction index variation, δn , caused

by thermal blooming and potentially other effects like turbulence. The general solution to Equation 4.5 is given by

$$\psi = \tilde{A}e^{ikz}, \quad (4.6)$$

where $\tilde{A} = |A|e^{-i\omega t}$, $k = 2\pi/\lambda$, ω is the angular frequency, and z is the distance in the direction of propagation. The refraction index variation, δn , caused by thermal blooming is given by

$$\delta n = \frac{\delta n}{\delta T} \Delta T = -\frac{n_o - 1}{T_o} \Delta T, \quad (4.7)$$

where n_o is the ambient refractive index, T_o is the ambient temperature, and ΔT is the temperature change in that particular portion of the atmosphere due to absorption.

This temperature change due to thermal blooming is described using the isobaric equation [14],

$$\frac{\partial \Delta T}{\partial t} = \frac{\alpha}{\rho C_p} I - (\mathbf{v} \cdot \nabla_{\perp}) \Delta T + \left(\frac{K}{\rho C_p} \nabla_{\perp}^2 \right) \Delta T, \quad (4.8)$$

The $\alpha/\rho C_p I$ term describes the heating effect from the laser, where α is the absorption coefficient in Equation 4.2, ρ is the density of air, C_p is the constant-pressure specific heat capacity, and I is the laser's irradiance. The $(\mathbf{v} \cdot \nabla_{\perp}) \Delta T$ term describes the convection effects in the air, where \mathbf{v} is the wind velocity, and ∇_{\perp} is the transverse gradient operator. The $\left(\frac{K}{\rho C_p} \nabla_{\perp}^2 \right) \Delta T$ term describes the conduction effects in the air, where K is the thermal conductivity. Equation 4.8 assumes that the atmospheric pressure remains constant when the propagating high-power laser increases the temperature.

In a situation where there is little or no wind, the conduction term in Equation 4.8 dominates. In this scenario, the thermal blooming effect can be modeled by a dimensionless scaling factor, e^{-D_c} . The D_c parameter is given by [15]

$$D_c = -\frac{n_T P \alpha z^2}{2\pi K n_o \alpha^2}, \quad (4.9)$$

where $\alpha z \ll 1$, n_T is $\partial n / \partial T$ in Equation 4.7, P is the laser power, and α is the beam radius.

In windy situations, the thermal blooming effect depends on the wind speed as depicted by the second term on the right in Equation 4.8. The wind, which blows across the propagation path, causes the air's temperature to increase downwind. This increase in temperature causes the air's refractive index to decrease, and the beam bends in the direction of the increasing refractive index upwind. When the wind blows in the transverse x direction and $\partial \Delta T / \partial t = 0$ (i.e., at steady state), the phase shift due to thermal blooming is given by [14]

$$\phi(x, y, z) = ik \int_0^z \delta n dz = -\frac{n_o - 1}{T_o} \frac{\alpha k z}{\rho C_p \nu} \int_{-\infty}^x I dx'. \quad (4.10)$$

The laser irradiance pattern, for a given ϕ , due to thermal blooming can be estimated by solving Equation 4.5 with the ray-optics limit using perturbation theory [14]. The solution to Equation 4.5 can be approximated to the first order by

$$I(x, y, z) = I_o \exp \left\{ -N_c \left[2 \frac{x}{a} e^{-\frac{x^2+y^2}{a^2}} + \frac{\sqrt{\pi}}{2} e^{-\frac{y^2}{a^2}} \left(1 - \frac{4y^2}{a^2} \right) \left[1 + \operatorname{erf} \left(\frac{x}{a} \right) \right] \right] \right\}. \quad (4.11)$$

where I_o is the irradiance of the unperturbed beam, and N_c is the beam irradiance distortion parameter accounting for the wind effects given by

$$N_c = \frac{(n_o - 1) \alpha P z^2}{\pi n_o \rho C_p T \nu a^3}. \quad (4.12)$$

The larger the N_c parameter, the more thermal blooming deforms the propagating beam's irradiance pattern into a crescent shape shown in Figure 4.4.1.

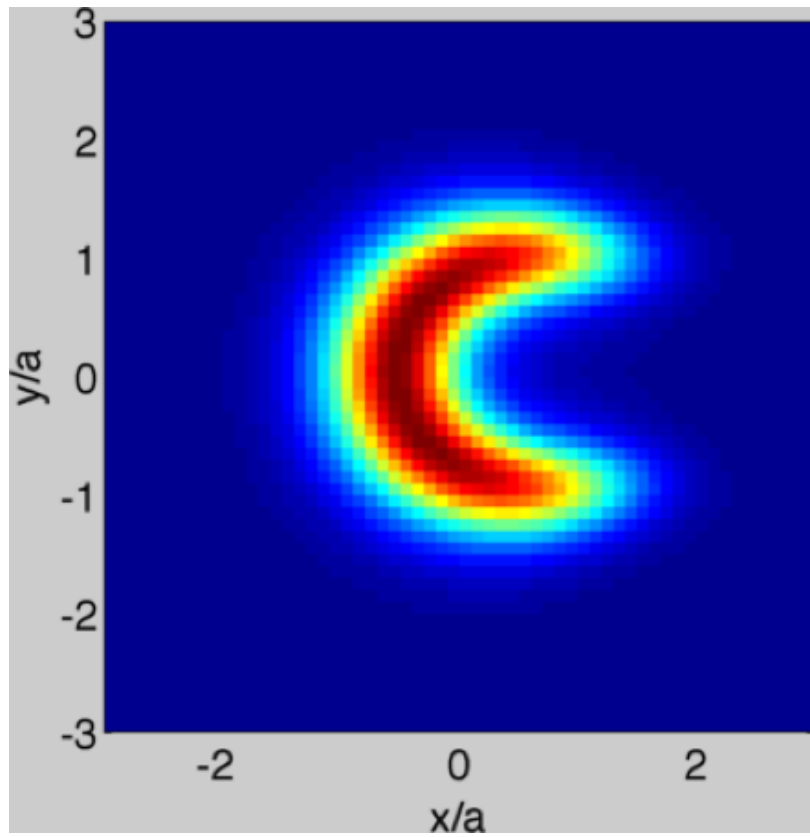


Figure 4.4.1: The laser irradiance pattern on the target due thermal blooming with $N_c = 1$. The color map represents the irradiance magnitude(i.e., dark red represents the highest intensity while light blue represents the lowest intensity).

CHAPTER 5:

Simulation Methods

Another mathematical form that is equivalent to Equation 4.5 is the time invariant Helmholtz equation given by

$$[\nabla^2 + k^2 n^2] \mathbf{E}(\mathbf{r}) = 0 , \quad (5.1)$$

where $\mathbf{E}(\mathbf{r})$ is the complex electric field of the propagating laser beam, $\mathbf{r} = x\mathbf{i} + y\mathbf{j} + z\mathbf{k}$, $k = 2\pi/\lambda$ is the wavenumber, and n is the index of refraction.

5.1 Diffraction Modeling

A solution to Equation 5.1 within the paraxial approximation is given by the Fresnel diffraction integral [16]

$$\mathbf{E}(\mathbf{r}_2) = \frac{e^{ik\Delta z}}{i\lambda\Delta z} \int_{-\infty}^{\infty} \mathbf{E}(\mathbf{r}_1) e^{i\frac{k}{2\Delta z} |\mathbf{r}_2 - \mathbf{r}_1|^2} d\mathbf{r}_1 , \quad (5.2)$$

where $\mathbf{r}_1 = x_1\mathbf{i} + y_1\mathbf{j}$ is the source plane vector, $\mathbf{r}_2 = x_2\mathbf{i} + y_2\mathbf{j}$ is the target vector coordinates, and Δz is the propagating distance between the source and target plane as illustrated by Figure 5.1.1.

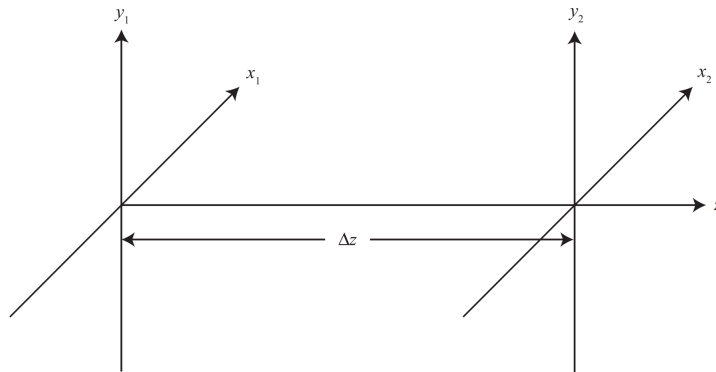


Figure 5.1.1: Optical wave propagation coordinate system. Source: [12].

It is very tedious to solve Equation 5.2 analytically and hence it would be advantageous to use a computer instead. For efficient computer simulation, Equation 5.2 can be expressed in Fourier transform terms as [12]

$$\mathbf{E}(\mathbf{r}_2) = \frac{e^{ik\Delta z} e^{i\frac{k}{2\Delta z}|\mathbf{r}_2|^2}}{i\lambda\Delta z} \mathcal{F}\{\mathbf{E}(\mathbf{r}_1) e^{i\frac{k}{2\Delta z}|\mathbf{r}_1|^2}\}_{|\mathbf{f}_1|}, \quad (5.3)$$

where $\mathbf{f}_1 = (f_{x1} = x_2/\lambda\Delta z, f_{y1} = y_2/\lambda\Delta z)$ is the source spatial frequency with grid spacing of δ_1 . For on-axis phase, the $e^{ik\Delta z}$ term can be ignored. Equation 5.2 can be expressed as another Fourier transform equation, which performs a convolution between the source plane field and the free space amplitude spread function, as [12]

$$\begin{aligned} \mathbf{E}(\mathbf{r}_2) &= \mathbf{E}(\mathbf{r}_1) \otimes \left[\frac{e^{ik\Delta z}}{i\lambda\Delta z} e^{i\frac{k}{2\Delta z}|\mathbf{r}_1|^2} \right], \\ \mathbf{E}(\mathbf{r}_2) &= \mathcal{F}^{-1} \left\{ \mathcal{F}\{\mathbf{E}(\mathbf{r}_1)\} \times \mathcal{F} \left\{ \frac{e^{ik\Delta z}}{i\lambda\Delta z} e^{i\frac{k}{2\Delta z}|\mathbf{r}_1|^2} \right\} \right\}, \end{aligned} \quad (5.4)$$

where the free space amplitude spread Fourier transform function is

$$\mathcal{F} \left\{ e^{ik\Delta z} e^{i\frac{k}{2\Delta z}|\mathbf{r}_1|^2} \right\} = e^{ik\Delta z} e^{-i\pi\lambda\Delta z|\mathbf{f}_1|^2}. \quad (5.5)$$

Substituting Equation 5.5 into Equation 5.4

$$\mathbf{E}(\mathbf{r}_2) = \mathcal{F}^{-1} \left\{ \mathcal{F}\{\mathbf{E}(\mathbf{r}_1)\} \times e^{ik\Delta z} e^{-i\pi\lambda\Delta z|\mathbf{f}_1|^2} \right\}, \quad (5.6)$$

Since Equation 5.4 performs two Fourier transforms, Equation 5.3 is desired for faster computational speed. Although Equation 5.4 is not as efficient, it compensates by introducing an additional parameter which provides grid spacing flexibility for the observation plane [12]. The equation implemented for the newly developed propagation model is based on Equation 5.4. The propagation model is implemented in Matlab to simulate incoherent and coherent beam combination considering diffraction, thermal blooming, turbulence, absorption and scattering effects.

Since the computer simulation only samples $\mathbf{E}(\mathbf{r}_1)$ at a fixed interval, it is difficult to obtain

accurate numerical computation of the Fresnel diffraction integral. Issues associated with sampling are:

1. Discrete samples on a finite-sized grid requires the spatial frequency to fulfill the Nyquist-Shannon sampling theorem, otherwise aliasing, rippling and smearing will occur in the spatial-frequency domain in addition to virtual periodic replication in the spatial domain.
2. Circular shifting of the samples can occur in the spatial domain (i.e., samples are time shifted so that the first sample coincides with the origin) to account for only positive indices. The reordering of spatial samples means that the samples in the spatial-frequency domain will be out of order, too.
3. The quadratic phase factor inside the Fresnel diffraction integral is not bandlimited and hence sufficient spatial resolution is required.

In addition, the geometry due to laser propagation also limits the observable spatial frequency content at the source plane when using Equation 5.3 for single step propagation due to the fixed grid spacing, $\delta_2 = \lambda \Delta z / N \delta_1$, at the target plane.

As mentioned earlier, Equation 5.4 introduces an additional scaling parameter by manipulating the quadratic phase factor which is inside the Fresnel diffraction integral [17], [18]:

$$\begin{aligned}
|\mathbf{r}_2 - \mathbf{r}_1|^2 &= r_2^2 - 2\mathbf{r}_1 \cdot \mathbf{r}_2 + r_1^2 \\
&= \left(r_2^2 + \frac{r_2^2}{m} - \frac{r_2^2}{m} \right) - 2\mathbf{r}_1 \cdot \mathbf{r}_2 + (r_1^2 + mr_1^2 - mr_1^2) \\
&= m \left[\left(\frac{r_2}{m} \right)^2 - 2 \left(\frac{\mathbf{r}_2}{m} \right) \cdot \mathbf{r}_1 + r_1^2 \right] + \left(1 - \frac{1}{m} \right) r_2^2 + (1 - m)r_1^2 \\
&= m \left| \left(\frac{\mathbf{r}_2}{m} \right) - r_1 \right|^2 - \left(\frac{1 - m}{m} \right) r_2^2 + (1 - m)r_1^2.
\end{aligned} \tag{5.7}$$

Substituting Equation 5.7 into Equation 5.2 yields

$$\begin{aligned}
\mathbf{E}(\mathbf{r}_2) &= \frac{e^{ik\Delta z}}{i\lambda\Delta z} \int_{-\infty}^{\infty} \mathbf{E}(\mathbf{r}_1) e^{i\frac{k}{2\Delta z} \left[m \left| \left(\frac{\mathbf{r}_2}{m} \right) - \mathbf{r}_1 \right|^2 - \left(\frac{1-m}{m} \right) r_2^2 + (1-m)r_1^2 \right]} d\mathbf{r}_1, \\
&= \frac{me^{ik\Delta z} e^{-i\left(\frac{k(1-m)}{2\Delta z m}\right)r_2^2}}{i\lambda\Delta z} \int_{-\infty}^{\infty} \frac{1}{m} \mathbf{E}(\mathbf{r}_1) e^{i\frac{k}{2\Delta z} (1-m)r_1^2} e^{i\frac{k}{2\Delta z} m \left| \left(\frac{\mathbf{r}_2}{m} \right) - \mathbf{r}_1 \right|^2} d\mathbf{r}_1, \\
\mathbf{E}(\mathbf{r}_2) &= e^{-i\left(\frac{k(1-m)}{2\Delta z m}\right)r_2^2} \times \mathcal{F}^{-1} \left\{ \mathcal{F} \left\{ \mathbf{E}(\mathbf{r}_1) e^{i\frac{k(1-m)}{2\Delta z} |\mathbf{r}_1|^2} \right\} \Big|_{\mathbf{f}_1=\mathbf{r}_1} \times e^{ik\Delta z} e^{-i\pi\lambda\frac{\Delta z}{m} |\mathbf{f}_1|^2} \right\}.
\end{aligned} \tag{5.8}$$

Equation 5.8 has the exact same convolution form as Equation 5.4 with \mathbf{r}_2 replaced by \mathbf{r}_2/m and Δz replaced by $\Delta z/m$. Since the quadratic phase factor inside the Fresnel diffraction integral is not bandlimited, the waveform that is to be Fourier transformed discretely needs to be sufficiently sampled in order to prevent aliasing. Hence for accurate simulation results, the grid spacing and the number of grid points are critical. The grid spacing, number of grid points, and propagation distance must fulfil the following constraints based on the Nyquist sampling theorem [12].

$$\delta_2 \leq \frac{\lambda\Delta z - D_2\delta_1}{D_1}, \tag{5.9}$$

$$N \geq \frac{D_1}{2\delta_1} + \frac{D_2}{2\delta_2} + \frac{\lambda\Delta z}{2\delta_1\delta_2}, \tag{5.10}$$

$$\left(1 + \frac{\Delta z}{R}\right)\delta_1 - \frac{\lambda\Delta z}{D_1} \leq \delta_2 \leq \left(1 + \frac{\Delta z}{R}\right)\delta_1 + \frac{\lambda\Delta z}{D_1}, \tag{5.11}$$

$$N \geq \frac{\lambda\Delta z_i}{\min(\delta_1\delta_n)^2}, \tag{5.12}$$

where δ_1 is the source grid spacing, δ_2 is the target grid spacing, D_1 is the source dimension, D_2 is the target dimension, and Δz_i is the maximum propagation distance. For a fixed δ_1 , δ_2 , and Δz , the number of grid points required according to Equation 5.10 will probably be very large resulting in long simulation run times. In order to shorten simulation run times, multiple partial propagation is usually preferred [12]. Using Equations 5.9 to 5.12, the maximum target plane spatial resolution is $\sim 20 \times 10^{-3}\text{m}$ requiring at least 512 grid points when a one meter diameter beam director with source plane spatial resolution of

$\sim 2 \times 10^{-3}\text{m}$ is focused onto a target five kilometer away (assuming that the maximum spot size is 0.5m). The maximum propagating distance is $\sim 800\text{m}$ and hence at least seven partial propagations are required to avoid aliasing. Using the parameters obtained, the beam's transverse diffraction term, ${}^{i/2k}\nabla_{\perp}^2\psi$, in Equation 4.5 for a spatially combined laser can be simulated without aliasing.

5.2 Thermal Blooming Modeling

The additional phase incurred due to thermal blooming described by Equation 4.5 will be implemented in the atmospheric propagation code. The change in temperature obtained using Equation 4.8 will cause a change in the ambient refractive index according to Equation 4.7, which alters the wavefront as shown by Equation 4.10 under the steady state assumption (i.e., $\partial\Delta T/\partial t = 0$). In order to simulate thermal blooming effects during laser propagation, the computation process is iterative because the change in phase depends on the laser intensity that is absorbed during the laser propagation, and vice versa as illustrated in Figure 5.2.1.

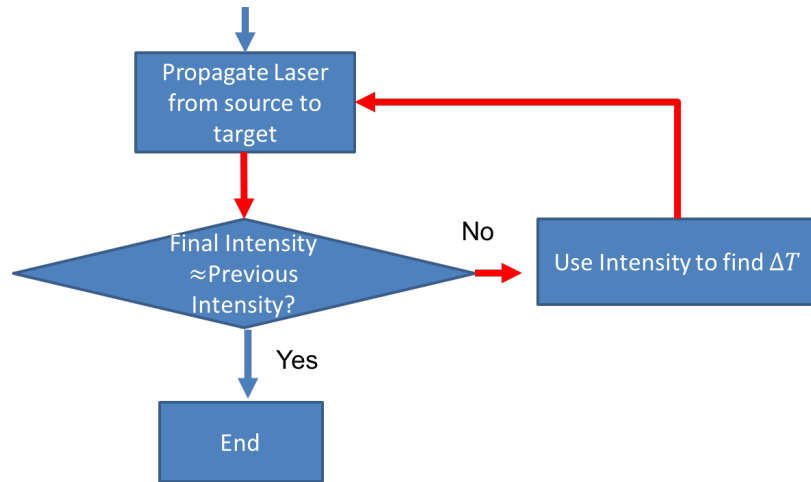


Figure 5.2.1: Method to obtain thermal blooming effects for laser propagating from source plane to target plane under the steady-state ($\frac{\partial\Delta T}{\partial t} = 0$) assumption.

Considering absorption, scattering, and thermal blooming effects, Equation 5.8 becomes

$$\mathbf{E}(\mathbf{r}_2) = e^A \times e^{-i\left(\frac{k(1-m)}{2\Delta z m}\right)r_2^2} \times \mathcal{F}^{-1} \left\{ \mathcal{F} \left\{ \mathbf{E}(\mathbf{r}_1) e^{i\frac{k(1-m)}{2\Delta z} |\mathbf{r}_1|^2} \right\} \right|_{\mathbf{f}_1=\mathbf{r}_1} \times e^{ik\Delta z} e^{-i\pi\lambda \frac{\Delta z}{m} |\mathbf{f}_1|^2} \right\}, \quad (5.13)$$

where $A = -\epsilon/2\Delta z + ik\delta n$.

The steady state assumption (i.e., $\partial\Delta T/\partial t = 0$) can be relaxed to incorporate transients. At each time step, the change in ambient temperature for all the phase screens are computed using the absorption term in Equation 4.5 neglecting the conduction effect (assume convection >> conduction) as

$$\Delta T_i = \int_t^{t+\delta t_i} \frac{\alpha}{\rho C_p} I dt \quad (5.14)$$

$$\Delta T_n = \sum_{k=0}^{i-1} \Delta T_k + \Delta T_i \quad (5.15)$$

where ΔT_i is the temperature change incurred due to the absorption of laser power during the time interval from t to $t + \delta t_i$ and ΔT_n is the total temperature change in ambient temperature at time t_n . During the same time interval, the convection effect due to wind can be modeled by shifting all the phase screens according to the wind magnitude and direction. This whole process is repetitively iterated until the target's intensity converges as illustrated by the Figure 5.2.2.

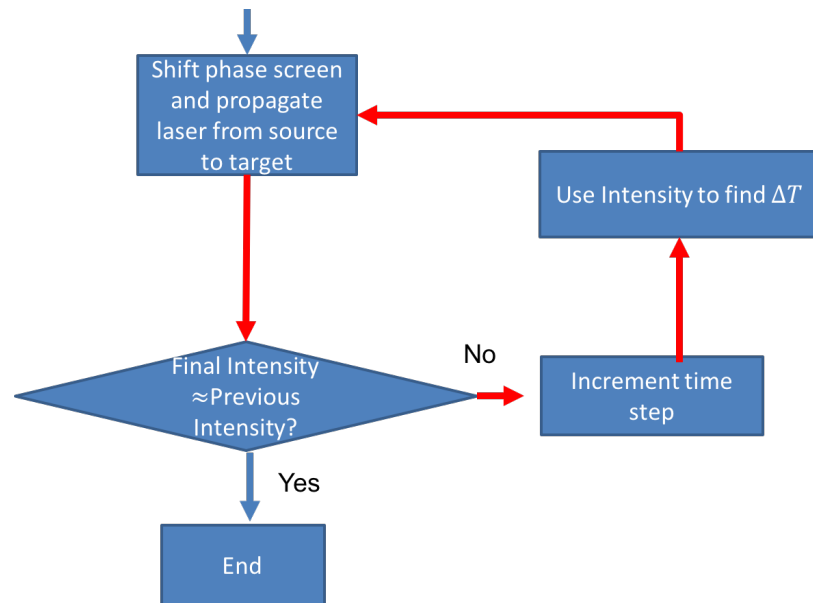


Figure 5.2.2: Method to obtain thermal blooming effects for laser propagating from source plane to target plane under relaxed steady state condition.

5.3 Incoherent Beam Combining Modeling

Equation 5.13, which models coherent sources only, can be modified to model an incoherent source by adding a random phase to each beamlet. For each time step, the random phase to each beamlet is changed. The target irradiance pattern is then obtained by averaging the target's irradiance pattern over several iterations until it converges.

5.4 Genetic Algorithm Modeling

The arrangement of beamlets at the beam director output aperture will affect the amount of laser intensity at the target especially for coherent beam combination. The enclosure of same radii and intensity beamlets within the beam director output aperture is similar to a circle packing algorithm, which is a very complex mathematical problem. Only certain circle packing arrangements have been proven to be optimal by mathematicians over the past few decades. Table 5.1 illustrates circle packing arrangements that are deemed or have been proven to be optimal. From Table 5.1, 14 or more beamlet packaging arrangements

are conjectured optimal illustrating the complexity of circle packing algorithm. For a given number of enclosed beamlets, the ratio of the beam director radius to the beamlet radius is shown in Table 5.1.








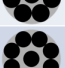

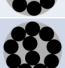




No of enclosed beamlets	Ratio of beam director radius to beamlet radius	Diagram	Remarks
1	1		Optimal (Trivial) Fill Factor: 100%
2	2		Optimal (Trivial) Fill Factor: 50%
3	~2.154		Optimal (Trivial) Fill Factor: 64.66%
4	~2.414		Optimal (Trivial) Fill Factor: 68.64%
5*	~2.701		Optimal Fill Factor: 68.54%
6*	3		Optimal Fill Factor: 66.67%
*Proved optimal by Graham in 1968			
7	3		Optimal (Trivial) Fill Factor: 77.78%
8* ¹	~3.304		Optimal Fill Factor: 73.28%
9* ¹	~3.613		Optimal Fill Factor: 68.95%
10* ¹	~3.813		Optimal Fill Factor: 68.78%
* ¹ Proved optimal by Pirl in 1969			
11* ²	~3.923		Optimal Fill Factor: 71.48%
* ² Proved optimal by Melissen in 1969			
12* ³	~4.029		Optimal Fill Factor: 73.92%
13* ³	4.236		Optimal Fill Factor: 72.45%
* ³ Proved optimal by Fodor in 1969			
14* ¹	~3.304		Conjectured Optimal Fill Factor: 74.74%

Table 5.1: Table illustrates how to pack beamlets of same radius optimally at the beam director output aperture. Source: [19].

Although optimal packing of same radii beamlets is important, the fill factor parameter will also affect the target's irradiance magnitude. Figure 5.4.1 and 5.4.2 illustrates how the fill factor can be different for a six beamlet configuration: one with six equal radius beamlets that is deemed to be optimally configured, and another that improve the fill factor by using

beamlets with two different radii. The fill factors for Figures 5.4.1 and 5.4.2 are 66.67% and 79.18% respectively. Relaxing the "equal radius" constraint may allow for more efficient packing using the same number of beamlets.

In addition, a genetic algorithm is used to vary the intensity of each beamlet radii group shown in Figure 5.4.3 to investigate if the target intensity will increase. A genetic algorithm is a probabilistic optimization method which involves mutating a randomly generated population of beamlet intensities towards a locally or globally optimal solution after multiple simulation iterations. Two randomly selected intensity sets are selected and propagated from source to target during each iteration, then the set that produced the lower target peak irradiance is recombined or mutated.

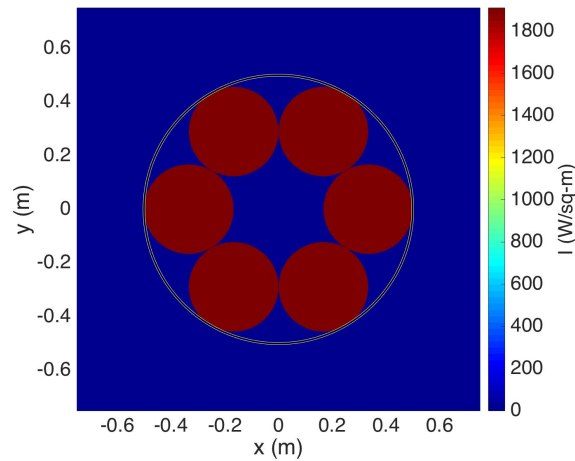


Figure 5.4.1: An example of six equal radii beamlets enclosed in a one meter diameter beam director. The color map indicates the beamlet's intensity.

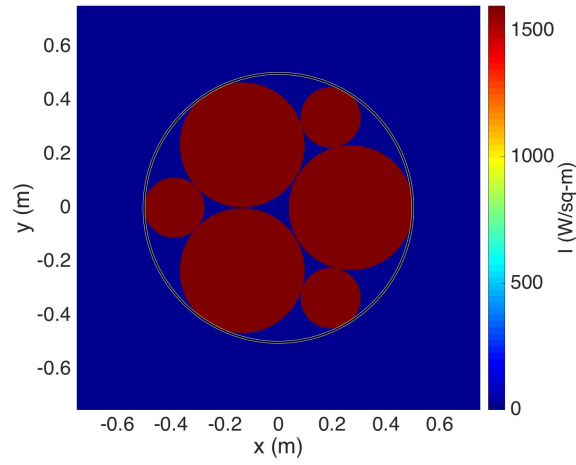


Figure 5.4.2: Another example of six beamlet configuration comprising of two different radii beamlets enclosed in a one meter diameter beam director. The color map indicates the beamlet's intensity.

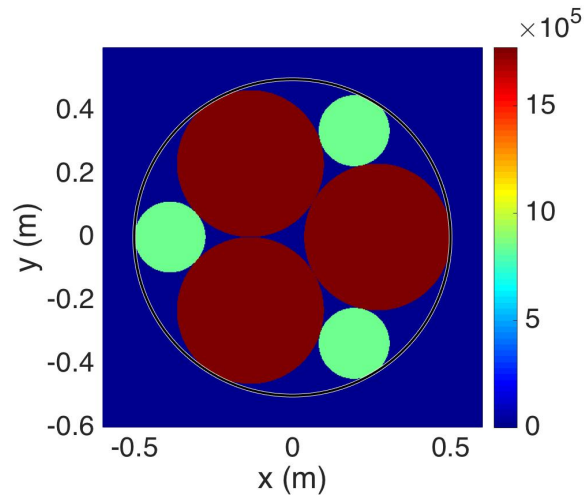


Figure 5.4.3: The intensity variation of different radii beamlet configuration at a one meter diameter beam director output aperture. The color map indicates the beamlet's intensity.

5.5 Model Validation

The best method to validate the newly developed atmospheric propagation model is to compare the simulation results with actual experimental data. Due to time and resource constraints, the simulation results obtained using the newly developed atmospheric propagation model will be compared with the results obtained from WaveTrain instead. All the WaveTrain results are provided by Dr. Pogue.

WaveTrain is a wave optics propagation code produced by MZA Associates Corporation available to U.S. government and their approved contractors only. WaveTrain simulates laser propagation by solving the paraxial wave equation 4.5 for coherent sources just like the newly developed propagation model. WaveTrain accounts for thermal blooming effects in a self-consistent transient manner. The simulation results obtained from WaveTrain are validated with experimental data and hence it can serve as a benchmark for the newly developed atmospheric propagation model [20]. The beam director is assumed to be an off-axis optical system on a stationary platform aiming at a stationary target during the entire model validation. The simulation parameters used for model validation are listed in Table 5.2.

Parameter	Value
Laser Wavelength	$3.8\mu\text{m}$
Target Distance	5km
Ambient temperature	300K
Absorption coefficient	10^{-5}m^{-1}
Scattering coefficient	10^{-5}m^{-1}
Cross-wind velocity	10m/s
Laser beamlet type	Uniform distribution

Table 5.2: Parameters used during model validation.

5.5.1 Diffraction Model

The diffraction model will be verified using both analytical means and WaveTrain. The verification is performed by filling the entire one meter beam director output aperture with a single 1kW laser source before verifying CBC and IBC diffraction effect. Since the laser power is low, the laser beam propagation path should not be affected by thermal blooming. The 1kW laser source at the beam director aperture is similar to a point source illuminating a one meter circular aperture and hence the target's irradiance pattern should comprise of diffuse circular discs known as Airy patterns. Since the target distance is much larger than the laser beam's wavelength, the wavefront arriving at the target can be approximated by plane wave. The target's two dimensional irradiance pattern for a one meter beam director diameter can be computed using the Fraunhofer, or far-field diffraction solution as

$$I = I_o \left(\frac{2J_1(\gamma)}{\gamma} \right)^2, \gamma \equiv \frac{1}{2}k \sin \theta, \quad (5.16)$$

where k is the spatial angular frequency of the laser beam, $J_1(\gamma)$ is the first order Bessel function, and I_o is the laser intensity at the beam director output aperture. The $J_1(\gamma)/\gamma$ term in Equation 5.16 is maximum as γ approaches zero (i.e., the irradiance is maximum at the center of the diffraction pattern). The first minimum occurs when $\gamma = 3.832$ which is offset from the center maximum point by

$$\Delta r \approx R \times \theta = R \times 1.22 \frac{\lambda}{D}, \quad (5.17)$$

where R is the target distance and D is the beam director diameter. Based on Equation 5.17, the offset distance from the central maximum to the first minimum should be 2.32 cm for a target distance of five kilometer. This offset distance will be compared to the simulation result. In addition, the normalized intensity cross sectional profile will also be compared with analytical ones. Once the simulation result matches the analytical computation, the results will then be compared with those from WaveTrain. After this, CBC and IBC diffraction and interference patterns will then be compared to the results obtained from WaveTrain. A bigger target spot size should be expected for IBC as the spot size is inversely proportional to the beamlet diameter unlike in the case for CBC where the target spot size is inversely proportional to the beam director diameter.

5.5.2 Thermal Blooming Model

After validating the diffraction model, the entire one meter beam director output aperture will be filled with a single 1MW laser source to verify the thermal blooming effect. The results obtained will be verified against WaveTrain. Upon successful thermal blooming validation, CBC configuration will then be verified against WaveTrain. If the IBC diffraction effect and CBC thermal blooming effect matches the WaveTrain results, a 1MW IBC results would be hypothesized to be right since WaveTrain can be verified for a coherent source only.

THIS PAGE INTENTIONALLY LEFT BLANK

CHAPTER 6:

Simulation Results

The lethality of a DE weapon depends on many factors; the ability to melt a hole on the target is one of them. This capability depends on the target's material, the laser's far field irradiance, the spot size, and the laser dwell time. The power delivered that goes into melting the target area is

$$P_{melt} = F \times P_{bucket} - P_{loss}, \quad (6.1)$$

where P_{bucket} is the laser power that has been focused into the so-called "bucket" that defines target area (after atmospheric losses), F is the fraction of laser power absorbed by the target (~ 0.2) and P_{loss} is the power loss due to conduction and radiation effects. The power-in-the-bucket parameter is

$$P_{bucket} = \int_{bucket} I dA, \quad (6.2)$$

where dA is an area element on the target, I is the irradiance on the target, and the integral is evaluated over the bucket area. The radiation loss is approximately

$$P_{rad} = \varepsilon \sigma A (T_{melt}^4 - T_{ambient}^4), \quad (6.3)$$

where ε is the blackbody emissivity of the target surface, σ is the Stefan-Boltzmann constant, A is the surface area that the laser beam heats, T_{melt} is the target's melting temperature, and $T_{ambient}$ is the ambient temperature. The conduction loss P_{con} shown in Figure 6.0.1 is approximately

$$P_{con} = \frac{k A_{ring} (T_{melt} - T_{ambient})}{\Delta x}, \quad (6.4)$$

where A_{ring} is the area through which heat is conducted away from the target area (for thin targets, it is the product of the melted hole circumference and the target's thickness), k is the thermal conductivity, and Δx is the distance of the induced temperature gradient ($\sim 2\text{cm}$) for an engagement lasting a few seconds.

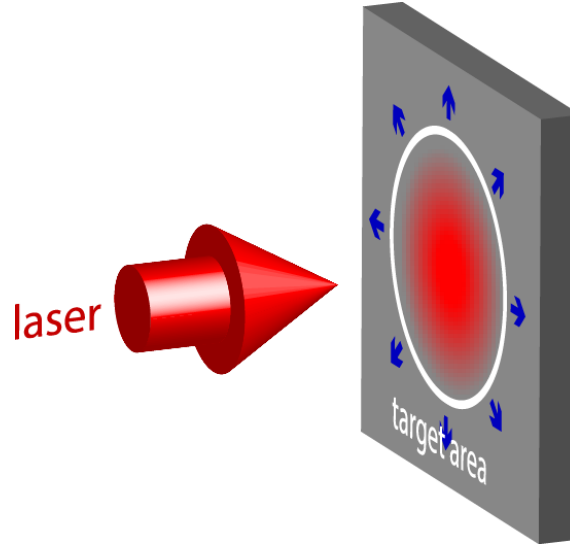


Figure 6.0.1: The conduction loss directions are indicated by the blue arrows.

The melting energy required is material dependent and is given by

$$Q_{melt} = Q_{heating} + Q_{trans}, \quad (6.5)$$

where $Q_{heating} = C_p m (T_{melt} - T_{ambient})$ is the heat energy required to reach the material's melting temperature, $Q_{trans} = m H_f$ is the energy required to melt the material, C_p is the material's heat capacity, H_f is the material's latent heat of fusion, and m is the mass of the melted target volume.

The required laser dwell time is

$$\tau_{dwell} = \frac{Q_{melt}}{P_{melt}}. \quad (6.6)$$

The average irradiance over the bucket is

$$I_{ave} = \frac{P_{bucket}}{A_{bucket}}, \quad (6.7)$$

where A_{bucket} is the area of the bucket. The minimum irradiance required to melt a certain volume of the target in a given τ_{dwell} is estimated as

$$I_{min} = \frac{P_{melt}}{A_{bucket}}. \quad (6.8)$$

According to Equations 6.2 to 6.8, the DE lethality depends highly on the laser dwell time, the minimum target irradiance, and the power-in-the-bucket. The minimum target irradiance is the amount of power per unit area required to melt the target while the power-in-the-bucket measures how much laser power has been focused onto a defined spot on the target.

Consider a target with the following properties in Table 6.1. In this case, the average irradiance required to create a 10cm hole on the target within eight seconds is $\sim 65 \text{ MW/m}^2$ and the amount of power-in-the-bucket required is $\sim 0.5 \text{ MW}$.

Aluminum properties	Value
Density, ρ	2700 kg/m^3
Thickness	0.02m
Melting temperature, T_{melt}	933K
Latent heat of fusion, H_f	400kJ/kg
Heat capacity, C_p	897J/kg-K
Thermal conductivity, k	237 W/m-K
Ambient temperature, $T_{ambient}$	300K
Emissivity, ε	0.05

Table 6.1: Target material made of aluminum. Source: [21].

Since the irradiance and power-in-the-bucket parameters are crucial for DE lethality, they will be used as a performance indicator during validation of the propagation model. Furthermore, the beam director fill factor affects the target's peak irradiance for coherent beam combination. Different fill factor configurations listed in Table 6.2 will be simulated.

No. of enclosed beamlets	Remarks
1	single beam
3	same radii beamlet with fill factor of $\sim 65\%$
6	same radii beamlet with fill factor of $\sim 67\%$
6	two different beamlet radii with fill factor of $\sim 79\%$
13	two different beamlet radii with fill factor of $\sim 84\%$

Table 6.2: Beamlet configurations used for simulation.

6.1 Diffraction Results

Figure 6.1.1 shows the beam director and target irradiance patterns due to a uniformly distributed 1kW laser source. According to Figures 6.1.2 and 6.1.3, the peak target irradiance is $\sim 2\text{MW/m}^2$ and the first null distance occurs 2.32cm away from the center maximum. The first null distance obtained from simulation matches the theoretical analysis performed in Chapter 5. Since the source irradiance pattern is symmetrical, the target's irradiance pattern must be symmetrical along the x-axis and y-axis as shown in Figures 6.1.2 and 6.1.3.

Figure 6.1.1 also shows a 10cm diameter bucket containing $\sim 840\text{W}$. The amount of power reaching the target plane is $\sim 900\text{W}$. This result is consistent with Equation 4.1 where $\sim 100\text{W}$ attenuation of the laser source is due to absorption and scattering effects.

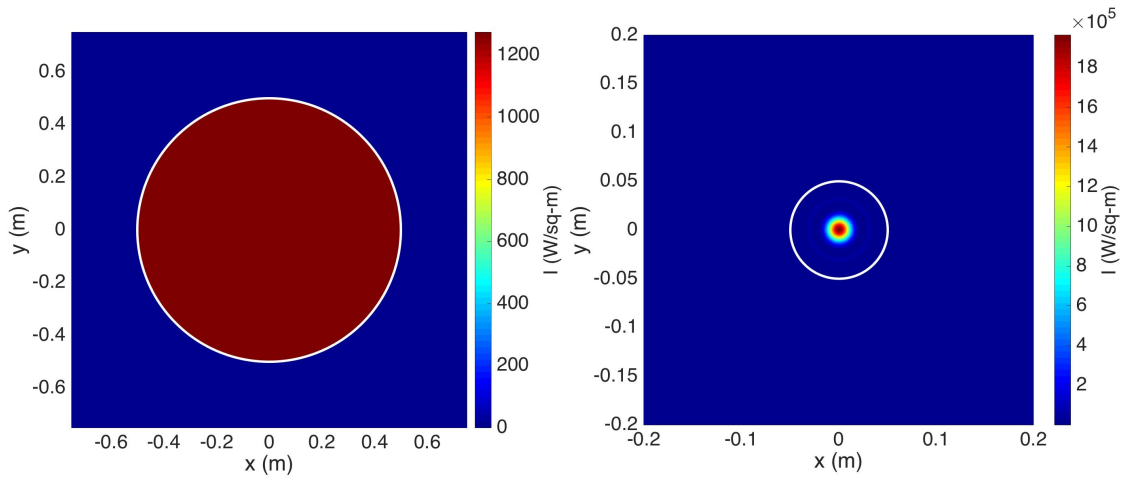


Figure 6.1.1: The irradiance pattern due to a 1kW single source at the beam director output aperture (left). The target irradiance pattern with a 10cm power-in-the-bucket circled in white (right). The color map represents the intensity.

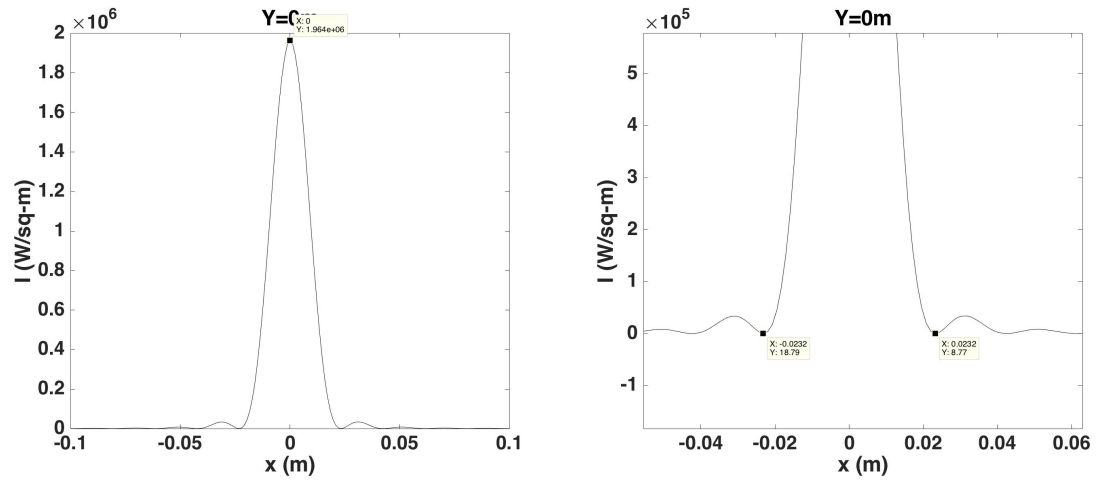


Figure 6.1.2: The cross-sectional intensity plot at the target plane for $Y=0$ cm (left). Magnified view of the cross-sectional plot showing the first null point (right).

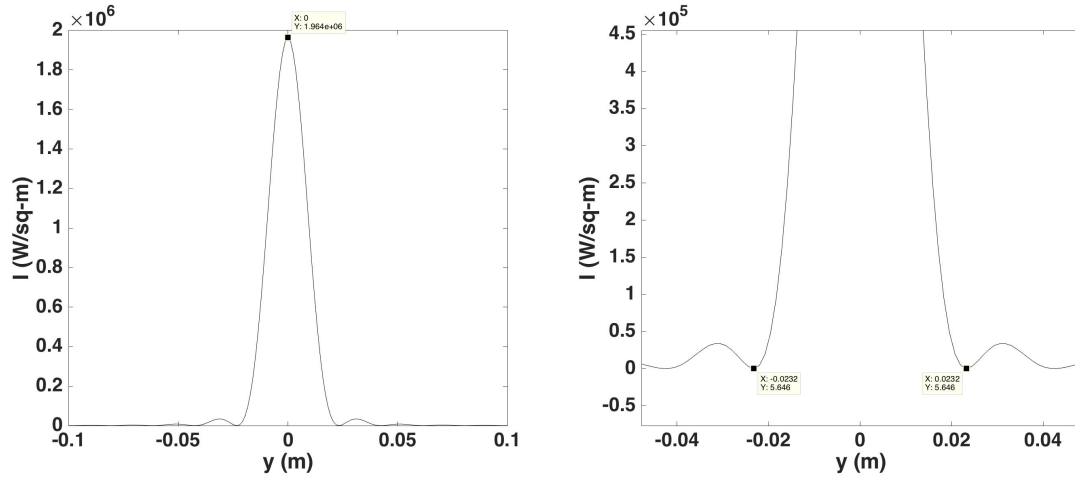


Figure 6.1.3: The cross-sectional intensity plot at the target plane for $X=0\text{cm}$ (left). Magnified view of the cross-sectional plot showing the first null point (right).

6.1.1 Coherent Beam Combination

Figure 6.1.4 shows the beam director irradiance pattern created by three uniformly distributed coherent beamlets with 1kW total output power. According to Figure 6.1.5, the target's irradiance patterns obtained from the propagation model and WaveTrain are essentially identical. From the cross-sectional plot in Figure 6.1.7, the peak target irradiance is $\sim 1.3\text{MW/m}^2$ and the first null distance along the x-axis occurs 2.44cm away from the center maximum. However, the first null distance along the y-axis occurs 2.69cm away from the center maximum as highlighted in Figure 6.1.6. The asymmetrical source irradiance pattern causes the null distance to be different along the different axes. Both the propagation model and WaveTrain contain $\sim 780\text{W}$ within a 10cm diameter bucket (circled in white in Figure 6.1.5). The amount of power reaching the target plane is $\sim 900\text{W}$ for both the propagation model and WaveTrain.

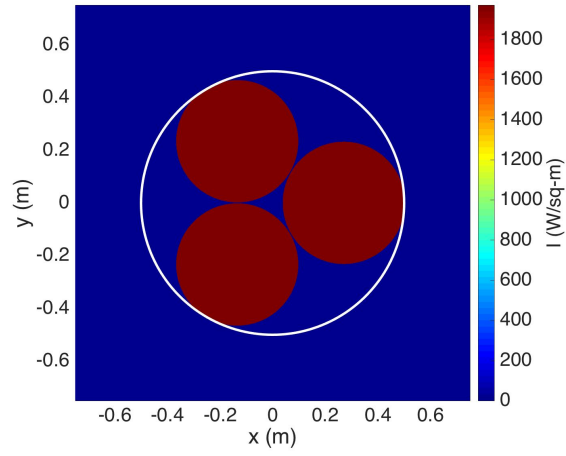


Figure 6.1.4: The irradiance pattern due to three coherent beamlets with 1kW output power at the beam director output aperture.

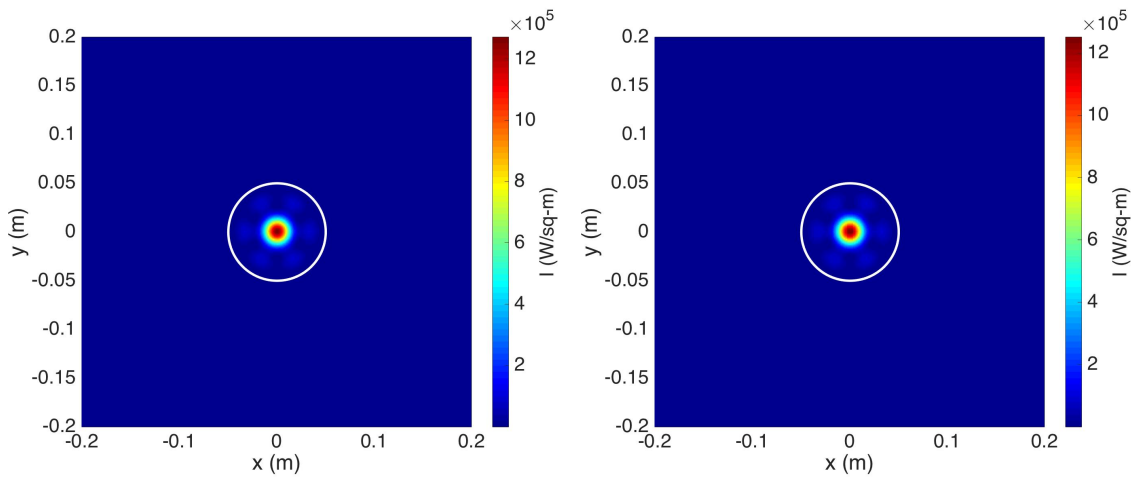


Figure 6.1.5: For the three coherent beamlets with 1kW output power, the target irradiance patterns for the propagation model (left) and Wave-Train (right). The 10cm diameter power-in-the-bucket is circled in white.

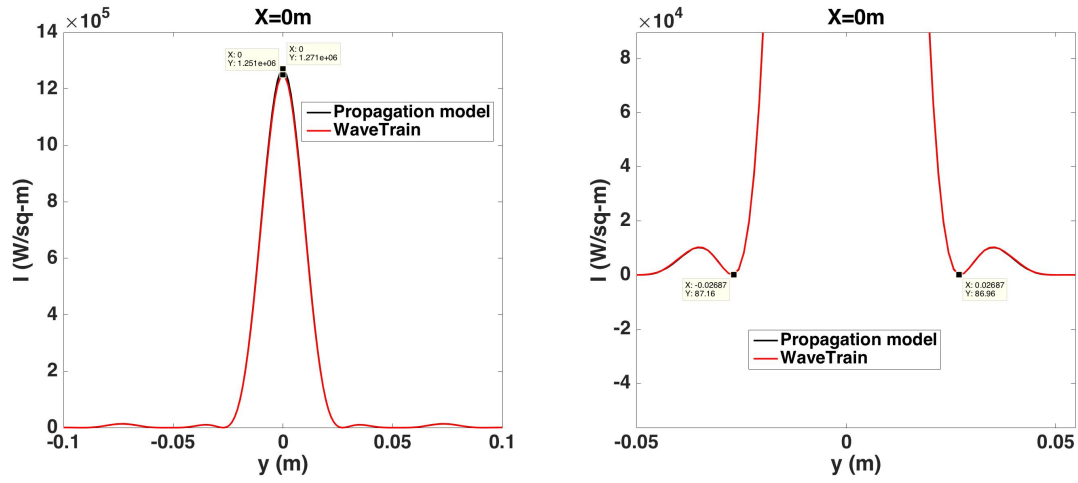


Figure 6.1.6: The cross-sectional intensity plot at the target plane for $X=0$ cm (left) as a result of the three coherent beamlets case. Magnified view of the cross-sectional plot showing the first null point (right).

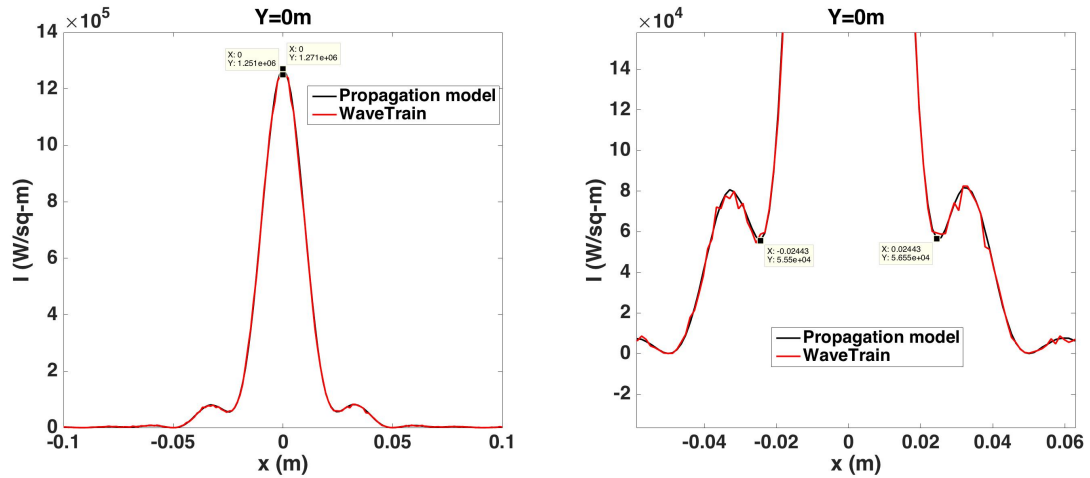


Figure 6.1.7: The cross-sectional intensity plot at the target plane for $Y=0$ cm (left) as a result of the three coherent beamlets case. Magnified view of the cross-sectional plot showing the first null point (right).

Figure 6.1.8 shows another beam director irradiance pattern created by 13 coherent beamlets of two different radii with 1kW output power. According to Figures 6.1.9, 6.1.10, and 6.1.11, the target irradiance patterns obtained from both the propagation model and WaveTrain have nearly identical structures and peak irradiance. From the cross-sectional plots in

Figures 6.1.10 and 6.1.11, the peak target irradiance is $\sim 1.7\text{MW/m}^2$ and the first null distance along the x and y-axes occurs $\sim 2.32\text{cm}$ away from the center maximum which happens to be the same as the single source configuration. Both the propagation model and WaveTrain contain $\sim 770\text{W}$ within a 10cm diameter bucket (i.e., circled in white) in Figure 6.1.9. The amount of power reaching the target plane is $\sim 900\text{W}$ for both the propagation model and WaveTrain.

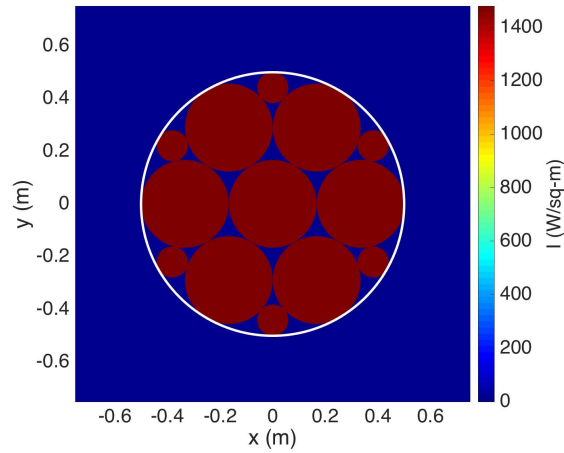


Figure 6.1.8: The irradiance pattern due to 13 coherent beamlets of two different radii with 1kW output power at the beam director output aperture.

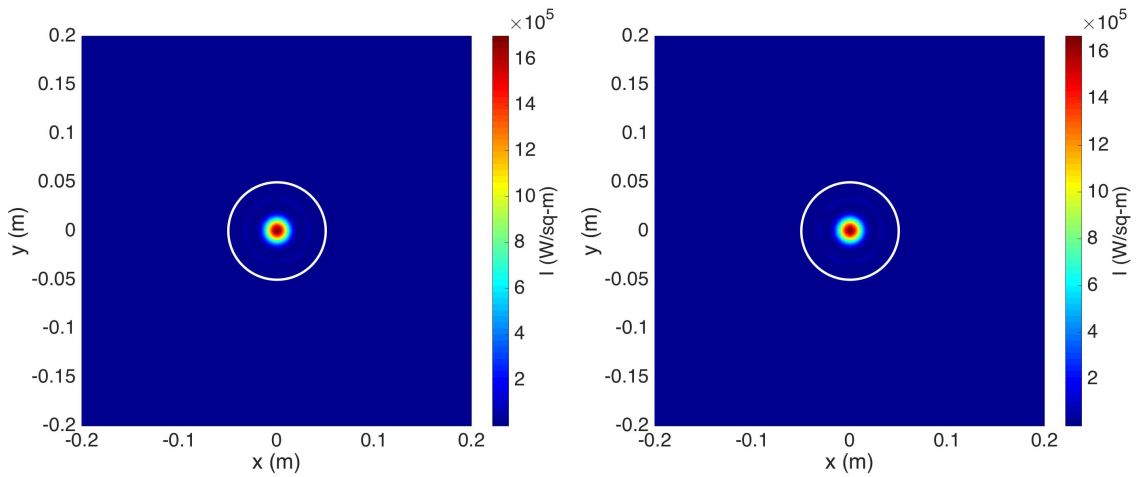


Figure 6.1.9: For the 13 coherent beamlets case with 1kW output power, the target irradiance patterns for the propagation model (left) and WaveTrain (right).

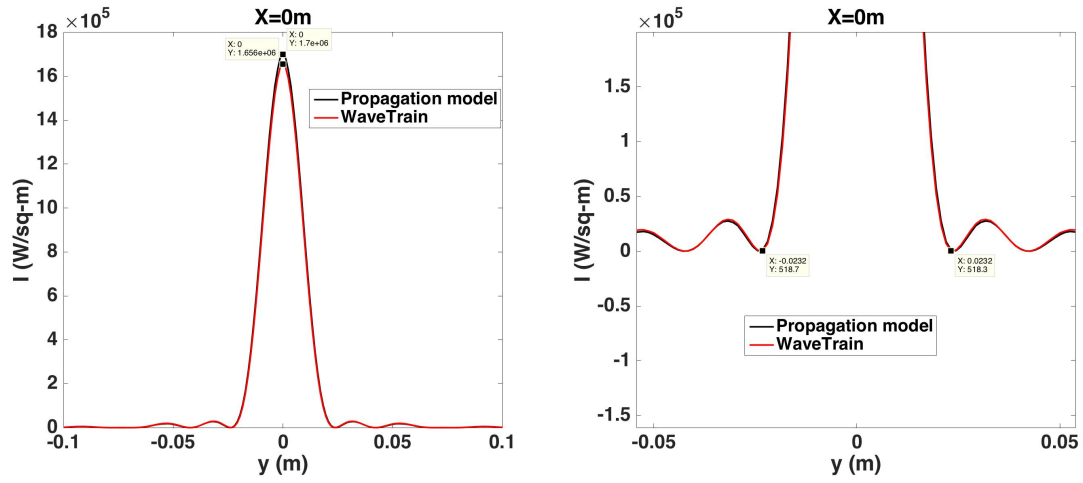


Figure 6.1.10: The cross-sectional intensity plot at the target plane for $X=0$ cm (left) as a result of the 13 coherent beamlets case. Magnified view of the cross-sectional plot showing the first null point (right).

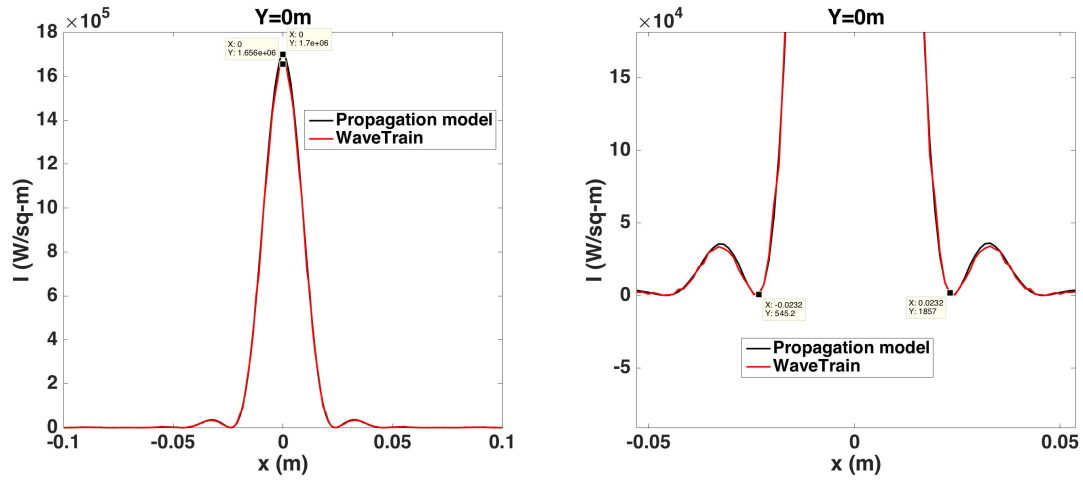


Figure 6.1.11: The cross-sectional intensity plot at the target plane for $Y=0$ cm (left) as a result of the 13 coherent beamlets case. Magnified view of the cross-sectional plot showing the first null point (right).

The simulation results obtained for coherent beam combination using the propagation model are summarized in Table 6.3.

Coherent beamlet configuration	Power in a 10 cm diameter bucket	Remarks
1	~840W	Symmetrical first null distance along x and y axes occurring 2.32cm away from the center maximum
3 same radii	~780W	Asymmetrical first null distance occurring 2.44cm and 2.69cm away from the center maximum for x and y axis, respectively.
13 beamlets with two different radii	~770W	Symmetrical first null distance along x and y axes occurring 2.2cm away from the center maximum

Table 6.3: 1kW coherent beamlet configuration results obtained using the propagation model.

6.1.2 Incoherent Beam Combination

Next, the following incoherent beamlet configurations will be validated by comparing its peak irradiance and spot size (i.e. radius measured from maximum irradiance to ~14% of peak irradiance) with corresponding results for the coherent configurations using the propagation model.

Figure 6.1.12 shows the irradiance pattern created by three incoherent beamlets with a total output power of 1kW. Comparing with Figure 6.1.5, the peak target irradiance is reduced by a factor of three. This reduction factor matches the number of enclosed beamlets according to Chapter 3. The target spot size shown in Figure 6.1.12 is ~1.9 times larger than the target spot size shown in Figure 6.1.5. Based on Table 5.1, this result is within ~12% from the expected ratio (i.e. 2.15). Although the peak irradiance is reduced by a factor of three, the power-in-the-bucket for this incoherent configuration is only ~20W less than the corresponding results for the coherent configurations.

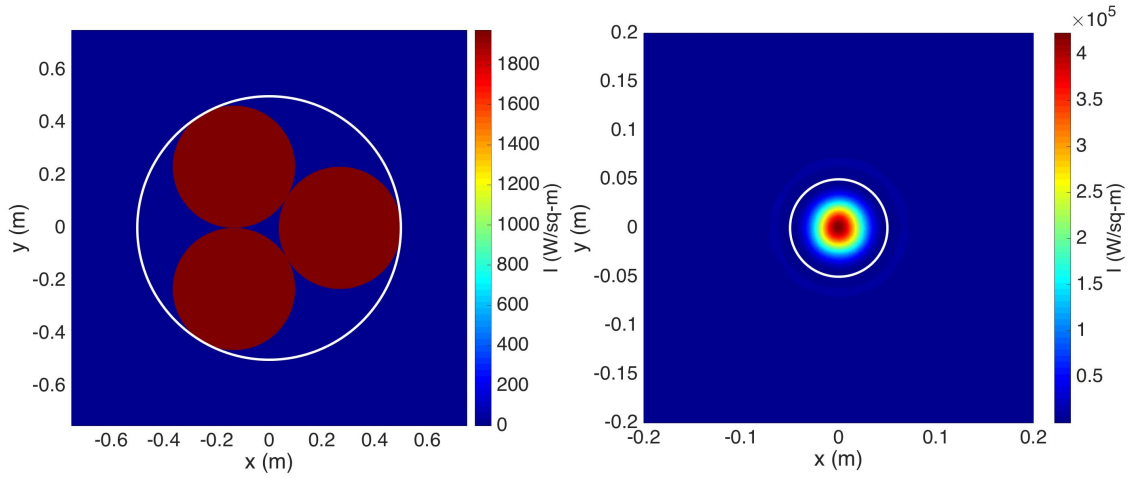


Figure 6.1.12: The irradiance pattern due to 3 incoherent beamlets with 1kW output power at the beam director output aperture.

Figure 6.1.13 shows an pattern created by 13 coherent beamlets of two different radii with 1kW total output power. Comparing with Figure 6.1.9, the peak target irradiance is reduced by a factor of ~ 8.2 . Based on Chapter 3, this result is reasonable as the reduction factor should be larger than the seven equal radius beamlet configuration. The target spot size shown in Figure 6.1.12 is approximately three times larger than the target spot size shown in 6.1.5. The power-in-the-bucket for this incoherent configuration is about $\sim 100\text{W}$ less than its coherent counterpart due to lower target peak irradiance and larger target spot size.

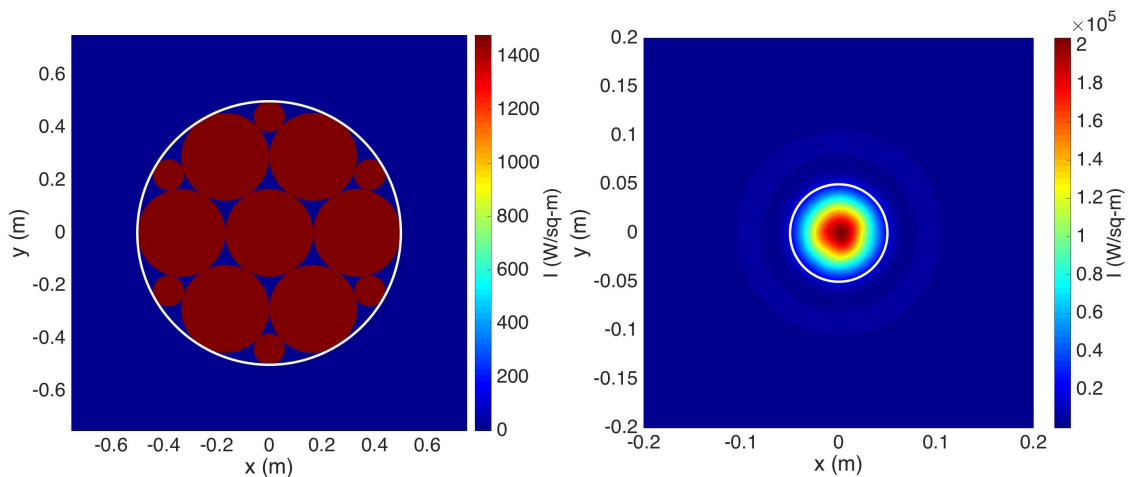


Figure 6.1.13: The irradiance pattern due to 13 incoherent beamlets of two different radii with 1kW output power at the beam director output aperture.

The simulation results obtained for incoherent beam combination using the propagation model are summarized in Table 6.4.

Incoherent beamlet configuration	Power in a 10 cm diameter bucket	$\frac{Spot\ Diameter_{IBC}}{Spot\ Diameter_{CBC}}$	$\frac{I_{peak_{CBC}}}{I_{peak_{IBC}}}$
3 same radii	~760W	~1.9	3
13 beamlets with two different radii	~670W	3	~8.3

Table 6.4: 1kW incoherent beamlet configuration results obtained using propagation model.

Based on both the analytical computation and WaveTrain results, the diffraction effects simulated in the propagation model are accurate.

6.2 Thermal Blooming

The laser output power at the beam director output aperture is now increased to 1MW so that thermal blooming effects become significant. Figure 6.2.1 shows the beam director irradiance pattern created by a uniformly distributed source with an output power of 1MW. According to Figure 6.2.2, the target irradiance patterns obtained from the propagation model and WaveTrain have similar structure but their peak target irradiance differs by ~28%. This difference is likely due to different thermal blooming methodology: WaveTrain uses a transient thermal blooming model while the propagation model assumes steady-state conditions. Both the propagation model and WaveTrain irradiance patterns are crescent shaped and bend into the direction of the transverse wind according to thermal blooming theory. Since the target irradiance patterns from the propagation model and WaveTrain are shifted away from the origin but symmetrical about the x axis, the power-in-the-bucket is computed by searching for the maximum power that is within the 10cm diameter bucket along the x-axis. Figure 6.2.2 shows a 10cm bucket containing ~580kW and ~620kW computed using the propagation model and WaveTrain results, respectively. Based on the power-in-the-bucket values, the single beam configuration can melt the target in less than eight seconds. Although their target peak irradiance differs by ~28%, the power-in-the

bucket differs by only $\sim 7\%$.

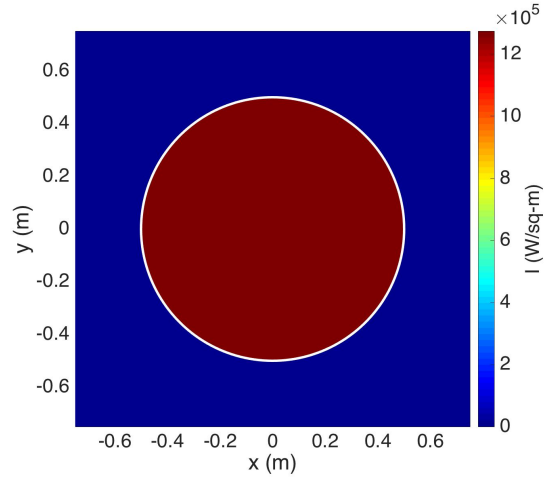


Figure 6.2.1: The irradiance pattern due to a single source with an output power of 1MW at the beam director output aperture. The color map indicates the intensity.

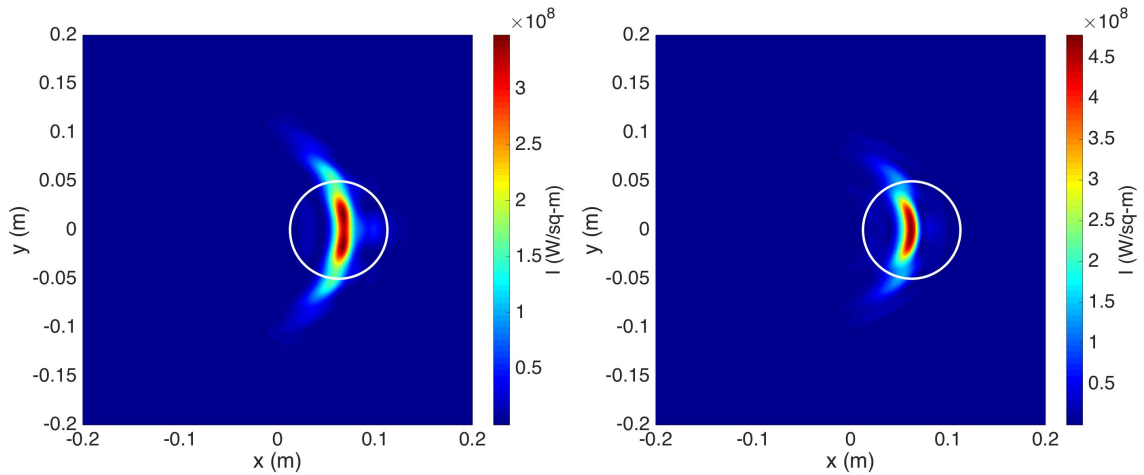


Figure 6.2.2: For the single beam case with 1MW output power, the target irradiance patterns for the propagation model (left) and WaveTrain (right).

Due to time constraints, only the single beam configuration will be simulated and analysed with the propagation model implementing transient thermal blooming. Comparing the results in Figure 6.2.3 to the results from WaveTrain in Figure 6.2.5, the target irra-

diance pattern are almost identical in structure and their peak target irradiance differs by only $\sim 6\%$. The power-in-the-bucket obtained using the propagation model with transient thermal blooming is $\sim 610\text{kW}$. This results only differs from WaveTrain by $\sim 2\%$. From the results obtained, it can be concluded that the propagation model with transient thermal blooming produces result that is within $\sim 6\%$ of results from WaveTrain. The runtime for the propagation model with transient thermal blooming is roughly similar to WaveTrain.

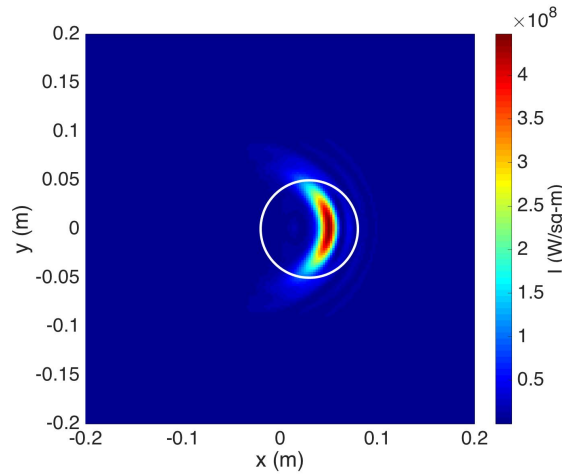


Figure 6.2.3: The target irradiance patterns for the propagation model implementing transient thermal blooming.

Figure 6.2.4 shows the beam director irradiance pattern created by three uniformly distributed coherent beamlets with 1MW output power. According to Figure 6.2.4, the target irradiance pattern obtained from the propagation model and WaveTrain are similar in structure and their peak target irradiance differs by only $\sim 15\%$, which is much less than the single beam configuration. Figure 6.2.5 shows a 10cm diameter bucket containing $\sim 340\text{kW}$ and $\sim 400\text{kW}$ computed using the propagation model and WaveTrain result, respectively. The power-in-the-bucket for this beamlet configuration may not be sufficient to melt the target in eight seconds. This beamlet configuration has $\sim 50\%$ less peak target irradiance and $\sim 40\%$ less power-in-the-bucket compared to the single beam configuration. A single beam that has equivalent fill area for the three beamlets configuration is shown in Figure 6.2.6. According to Figure 6.2.6, the peak irradiance is $\sim 200\text{MW/m}^2$ and the power-in-the-bucket computed is $\sim 450\text{kW}$. The three equal radius beamlets configuration has $\sim 18\%$ less peak target irradiance and $\sim 26\%$ less power-in-the-bucket compared to its equivalent fill area

single beam.

Since the two models treat thermal blooming differently, it is not surprising that they produce different results. Nevertheless, both models have peak irradiances within $\sim 30\%$ and power-in-the-bucket within $\sim 15\%$ of each other. The performance of the remaining beamlet configurations will be evaluated using the propagation model except when the arrangement of beamlets becomes complex (i.e., 13-beamlet configuration) as the runtime is significantly faster than WaveTrain.

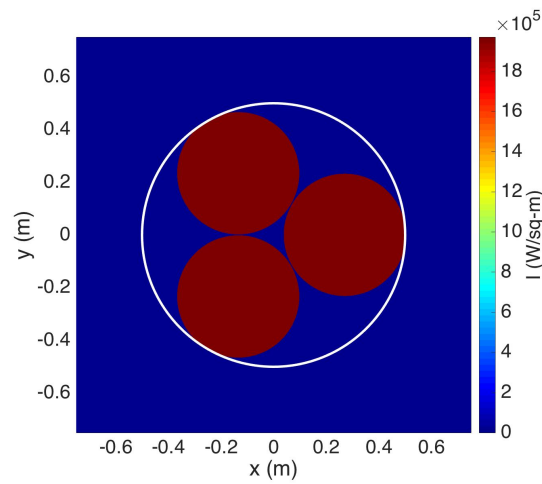


Figure 6.2.4: The irradiance pattern due to three equal radii coherent beamlets with 1MW output power at the beam director output aperture.

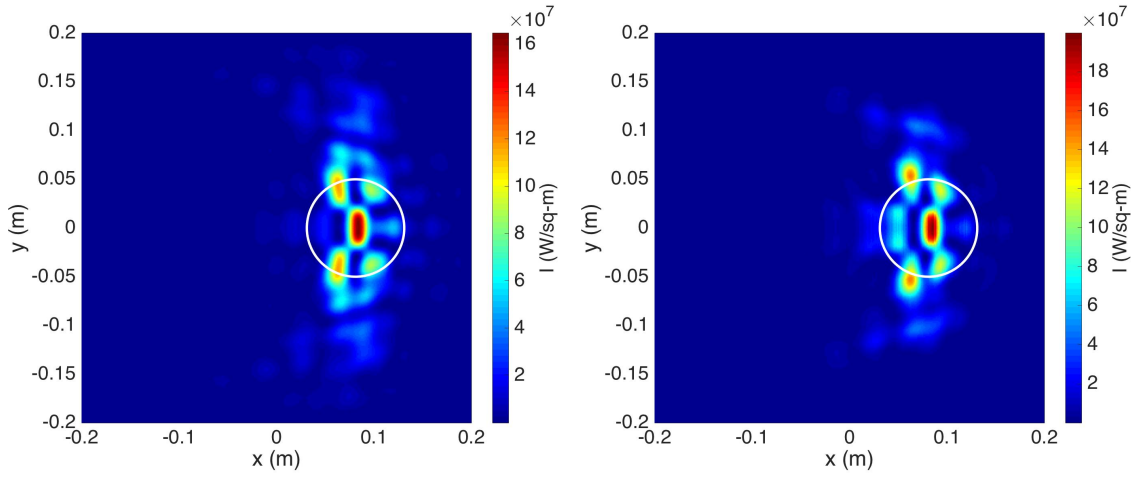


Figure 6.2.5: For the three equal radii coherent beamlets case with 1MW output power, the target irradiance patterns for the propagation model (left) and WaveTrain (right).

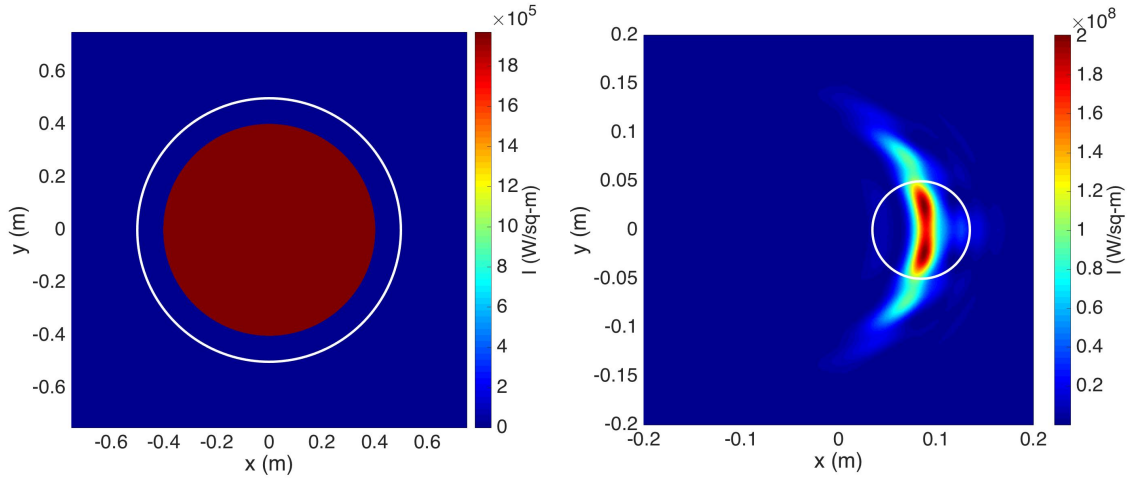


Figure 6.2.6: A single beam at the beam director aperture with the same fill area and output power as the three equal radii, coherent beamlets configuration (left). The target irradiance pattern obtained using the propagation model (right).

Figure 6.2.7 shows the beam director irradiance pattern created by six uniformly distributed beamlets with 1MW output power. According to Figure 6.2.7, the target peak irradiance is $\sim 150\text{MW/m}^2$ and the power-in-the-bucket computed is 360kW. Based on the power-in-

the-bucket, this beamlet configuration may requires more than eight seconds to melt the target. This beamlet configuration has $\sim 56\%$ less peak target irradiance and $\sim 38\%$ less power-in-the-bucket compared to the single beam configuration. Although the fill factor ratio difference between this case and the three equal beamlets configuration is only $\sim 2\%$, their relative peak irradiances differ by $\sim 8\%$ and the powers-in-bucket differ by $\sim 7\%$. Thus, the beamlet arrangement with respect to the transverse wind and the fill factor ratio is important.

A single beam that has equivalent fill area for the six beamlets configuration is shown in Figure 6.2.8. According to Figure 6.2.8, the peak irradiance is $\sim 210\text{MW/m}^2$ and the power-in-the-bucket is $\sim 460\text{kW}$. The six equal radius beamlets configuration has $\sim 27\%$ less peak target irradiance and $\sim 22\%$ less power-in-the-bucket compared to its equivalent fill area single beam.

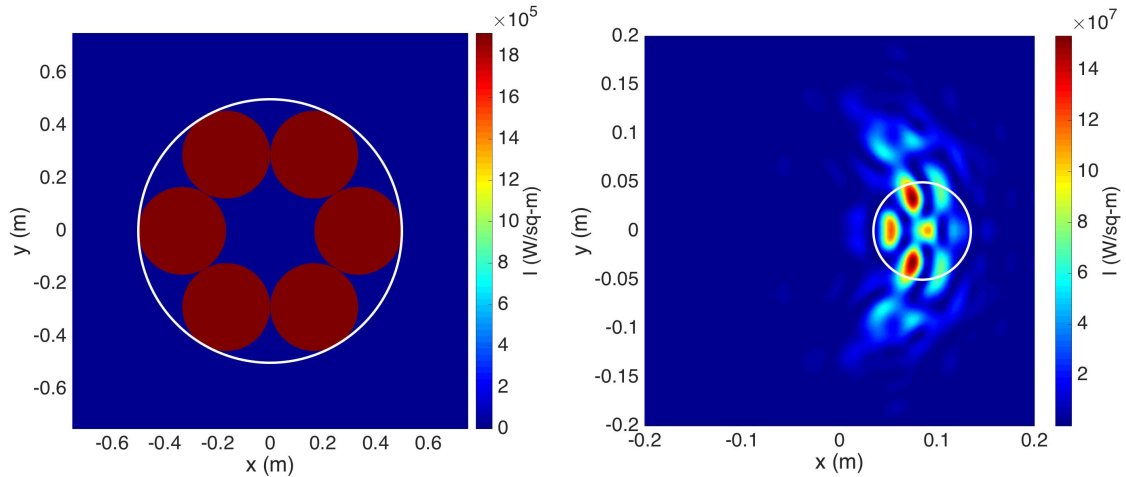


Figure 6.2.7: The irradiance pattern due to six equal radii coherent beamlets with 1MW output power at the beam director output aperture (left). The target irradiance pattern with a 10cm power-in-the-bucket circled in white (right).

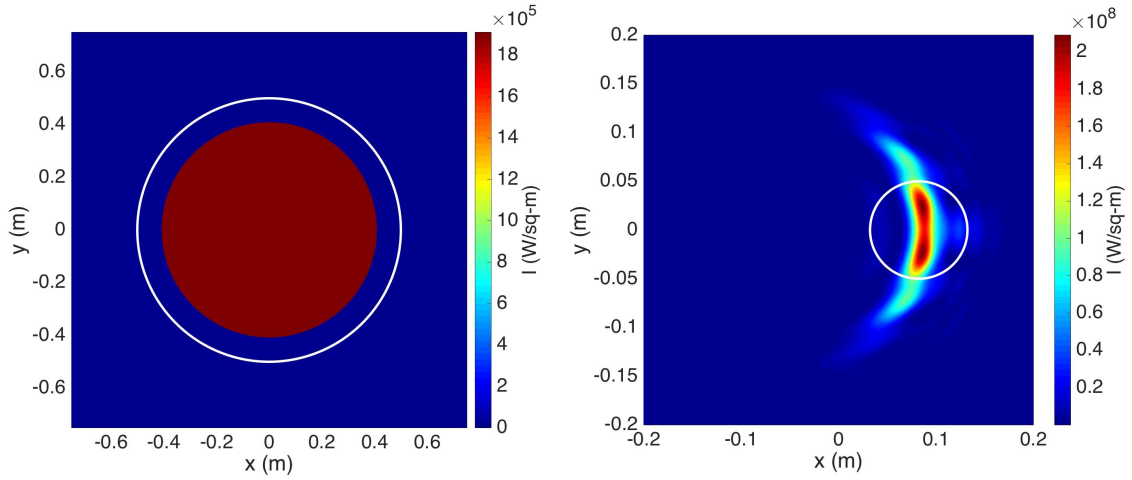


Figure 6.2.8: A single beam at the beam director aperture with the same fill area and output power as the six equal radii, coherent beamlets configuration (left). The target irradiance pattern obtained using the propagation model (right).

To further investigate the effects of fill factor, another six beamlets configuration shown in Figure 6.2.9 with two different radii and a total output power of 1MW is tested. According to Figure 6.2.9, the target peak irradiance is $\sim 170 \text{ MW/m}^2$ and the power-in-the-bucket computed is 310kW. Based on the power-in-the-bucket, this beamlet configuration requires more than eight seconds to melt the target. This beamlet configuration has $\sim 51\%$ less peak target irradiance and $\sim 47\%$ less power-in-the-bucket compared to the single beam configuration. This beamlet configuration has slightly more peak irradiance but less power-in-the-bucket compared to the six equal radii coherent beamlet. The decrease in power-in-the-bucket may be due to the asymmetrical source of this beamlet configuration with respect to the wind.

A single beam that has equivalent fill area for the six beamlets with two different radius configuration is shown in Figure 6.2.10. According to Figure 6.2.10, the peak irradiance is $\sim 260 \text{ MW/m}^2$ and the power-in-the-bucket computed is $\sim 510 \text{ kW}$. The six different radii coherent beamlets configuration has $\sim 39\%$ less peak target irradiance and $\sim 39\%$ less power-in-the-bucket compared to its equivalent single beam configuration.

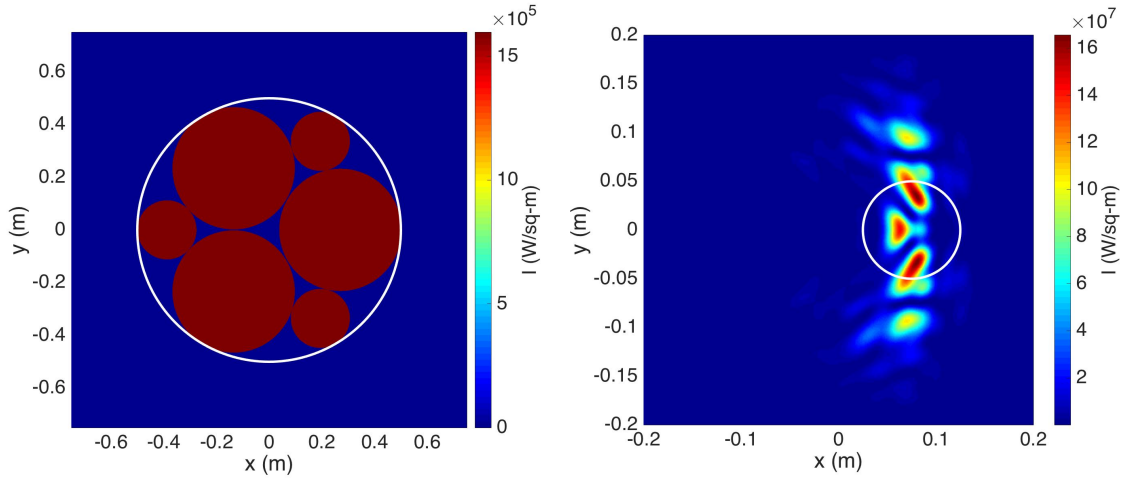


Figure 6.2.9: The irradiance pattern due to six coherent, different radii beamlets with 1MW output power at the beam director output aperture (left). The target irradiance pattern with a 10cm power-in-the-bucket circled in white (right).

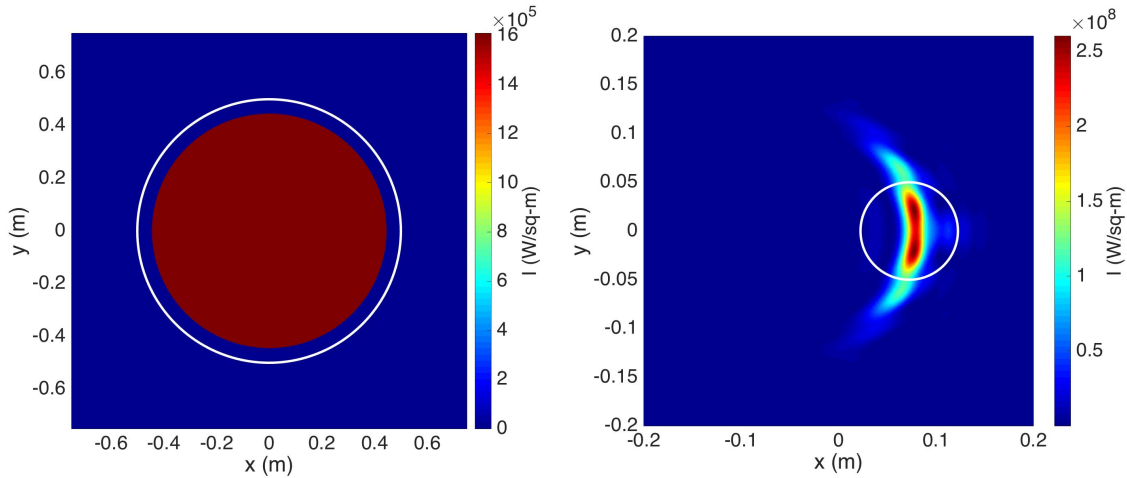


Figure 6.2.10: A single beam at the beam director aperture with the same fill area and output power as the three beamlets configuration (left). The target irradiance pattern obtained using the propagation model (right).

Next, 13 beamlets with two different radius and a output power of 1MW shown in Figure 6.2.11 is tested. This beamlet configuration is symmetrical about transverse wind direction and has fill factor slightly more than six beamlet shown in Figure 6.2.9. Accord-

ing to Figure 6.2.11, the target peak irradiance is $\sim 260 \text{ MW/m}^2$ and the power-in-the-bucket computed is 410kW. Based on the power-in-the-bucket, this beamlet configuration may require about eight seconds to melt the target. This beamlet configuration has $\sim 25\%$ less peak target irradiance and $\sim 29\%$ less power-in-the-bucket compared to the single beam configuration. This beamlet configuration has the closest peak irradiance, power-in-the-bucket, and irradiance pattern compared to the single beam configuration (i.e., best peak irradiance and power-in-the-bucket among all the other configurations). This result illustrates the importance of beamlet symmetry at the beam director output aperture and fill factor ratio.

A single beam that has equivalent fill area for the 13 beamlets with two different radius configuration is shown in Figure 6.2.13. According to Figure 6.2.13, the peak irradiance is $\sim 280 \text{ MW/m}^2$ and the power-in-the-bucket computed is $\sim 520 \text{ kW}$. This configuration has $\sim 7\%$ less peak target irradiance and $\sim 21\%$ less power-in-the-bucket compared to its equivalent single beam configuration. The 13 different radii coherent beamlets configuration also has the best peak irradiance and power-in-the-bucket among all the other configurations when compared to their equivalent fill area single beams.

As mentioned previously, this beamlet configuration's irradiance pattern will be compared to WaveTrain. Based on Figures 6.2.11 and 6.2.12, the irradiance patterns are almost identical and hence the irradiance pattern for any beamlet configurations obtained using the atmospheric should be roughly identical to WaveTrain.

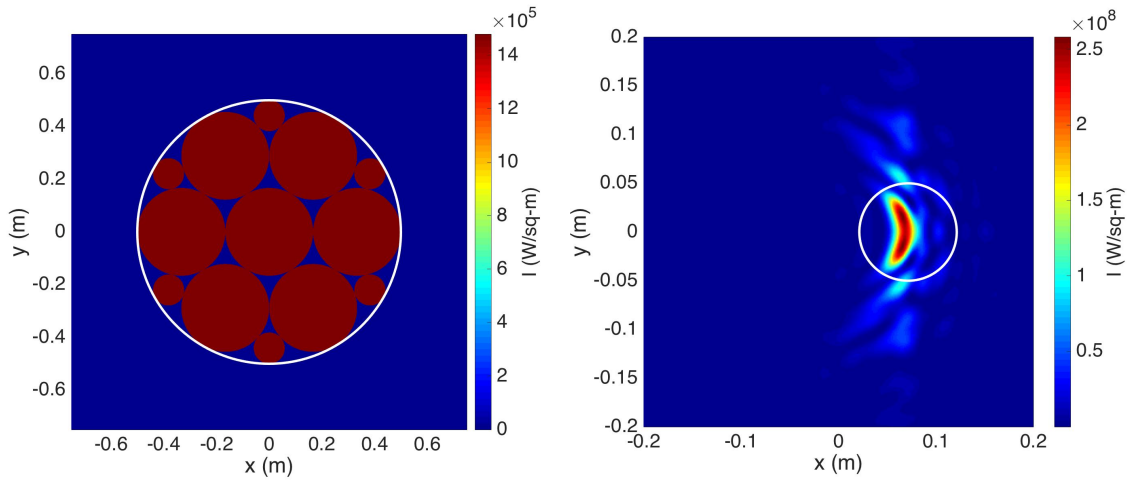


Figure 6.2.11: The irradiance pattern due to 13 coherent, different radii beamlets with 1MW output power at the beam director output aperture (left). The target irradiance pattern with a 10cm power-in-the-bucket circled in white (right).

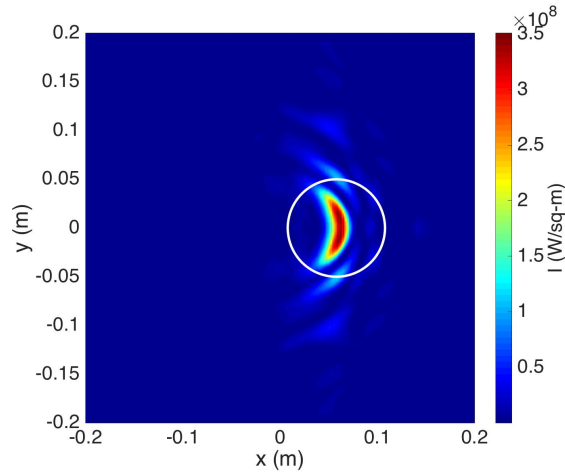


Figure 6.2.12: The target irradiance pattern with a 10cm power-in-the-bucket circled in white obtained using WaveTrain.

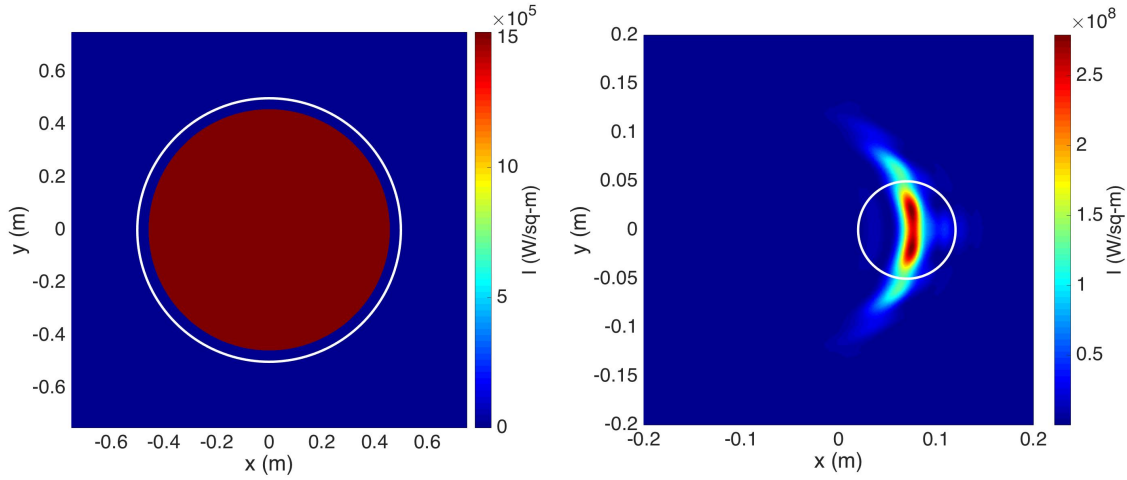


Figure 6.2.13: A single beam at the beam director aperture with the same fill area and output power as the three beamlets configuration (left). The target irradiance pattern obtained using the propagation model (right). The color map indicates the intensity.

6.3 Genetic Algorithm

The genetic algorithm is next used to investigate if higher peak irradiance can be obtained by varying the intensities of beamlets with different radii. Therefore the genetic algorithm is configured to iterate over different beamlet intensities to optimize the peak target irradiance. The six coherent beamlets with different radii shown in Figure 6.2.9 is passed to the genetic algorithm to search for maximum peak target irradiance. As shown in Figure 6.3.1, the peak target irradiance is $\sim 190 \text{ MW/m}^2$ and the power-in-the-bucket computed is 340kW. Based on the power-in-the-bucket, this beamlet configuration still requires more than eight seconds to melt the target. This beamlet configuration has $\sim 7\%$ less peak target irradiance and $\sim 41\%$ less power-in-the-bucket compared to the single beam configuration. There is an improvement of $\sim 6\%$ in peak irradiance and power-in-the-bucket compared to the constant intensity beamlet configuration. Comparing their performance with their equivalent fill area single beam configuration, there is an improvement of $\sim 12\%$ in peak irradiance and $\sim 6\%$ in power-in-the-bucket.

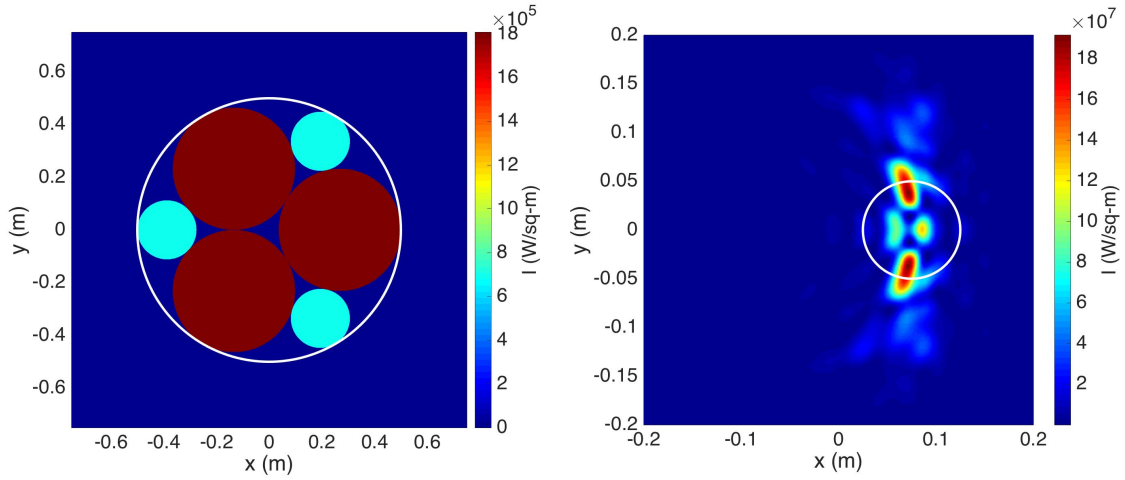


Figure 6.3.1: The irradiance pattern due to six coherent beamlets with two different radii and intensity at the beam director output aperture.

Next, the genetic algorithm is configured to optimize the peak target irradiance for the 13 coherent beamlets with different radii shown in Figure 6.2.11. According to Figure 6.3.2, the peak target irradiance is $\sim 290 \text{ MW/m}^2$ and the power-in-the-bucket computed is 400kW. Based on the power-in-the-bucket, this beamlet configuration still requires about eight seconds to melt the target. This beamlet configuration has $\sim 16\%$ less peak target irradiance and $\sim 30\%$ less power-in-the-bucket compared to the single beam configuration. There is an improvement of $\sim 9\%$ in peak irradiance but a reduction of $\sim 1\%$ in power-in-the-bucket compared to the constant intensity beamlet configuration. Comparing their performance with their equivalent fill area single beam configuration, there is an improvement of $\sim 11\%$ in peak irradiance and reduction of $\sim 2\%$ in power-in-the-bucket.

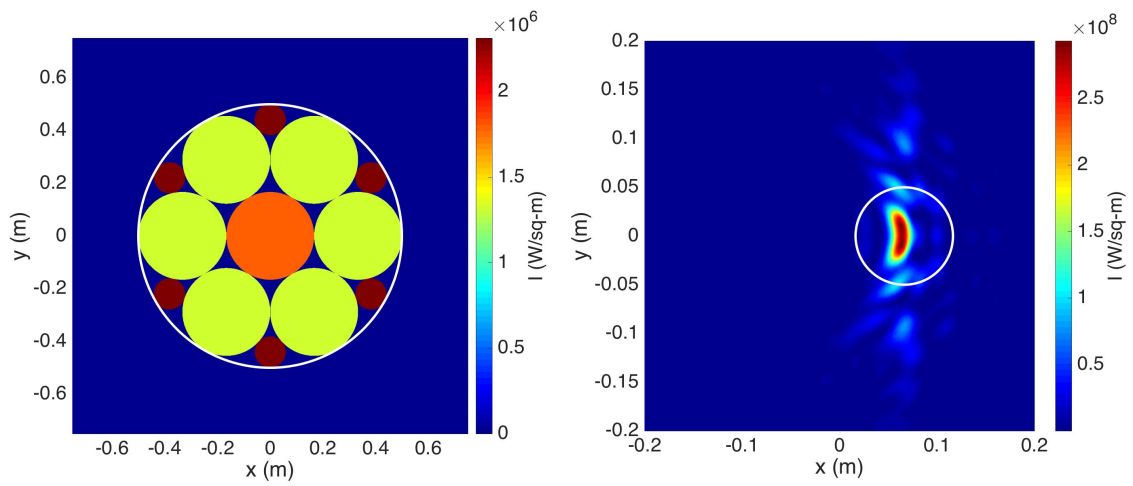


Figure 6.3.2: The irradiance pattern due to 13 coherent beamlets of two different radii and intensity with 1MW output power at the beam director output aperture.

THIS PAGE INTENTIONALLY LEFT BLANK

CHAPTER 7:

Conclusions

A new steady-state thermal blooming diffraction code has been developed for this thesis. This new code can analyze coherent beam combination, providing a solution that produces higher peak target irradiance for a given configuration of beamlets with different radii and irradiances, and computes faster than WaveTrain by a factor of three.

7.1 Comparison with Analytical and WaveTrain Results

For diffraction effects, the propagation model's results concur with analytical and WaveTrain results for a coherent source that has been focused onto a target five kilometer away. For thermal blooming effects, the peak irradiances obtained from the propagation model is within ~30% of WaveTrain and the power-in-bucket computed using the propagation model is within ~15% of WaveTrain too. This thermal blooming results are considered to be acceptable for these extreme cases since each code uses a different thermal blooming model.

7.2 Beamlet configuration with constant irradiance

Based on the target with material properties in Table 6.1, all beamlet configurations in Table 6.2 have sufficient irradiance to melt the target but insufficient power-in-the bucket to melt a 10cm hole within eight seconds except for the single-beam and 13-beamlet configuration. In fact, the 13-beamlet configuration not only has an irradiance pattern that resembles its equivalent fill factor area single beam but also the highest peak irradiance and power-in-the-bucket rating. Therefore the 13-beamlet configuration is considered the best among the tested configurations. For practical implementation, the alignment and beam control for the 13-beamlet configuration will be complex.

7.3 Beamlet configuration with varying irradiance

For both the six-beamlet and 13-beamlet configurations, there was a slight difference in the power-in-the-bucket compared to the corresponding cases with constant beamlet irradiance. Using the genetic algorithm to search for higher peak target irradiance, there was an improvement of $\sim 10\%$ in both the six-beamlet and 13-beamlet configurations. In fact, the 13-beamlet configuration has $\sim 8\%$ higher target peak irradiance than its equivalent fill area single beam. If higher peak irradiance is required, this configuration should be selected instead of the same intensity configuration.

7.4 Future Work

The current propagation model could be improved to incorporate the transient model described in Chapter 5 instead of using the steady-state condition. The implementation of the transient thermal blooming model will also enable the current propagation model to incorporate turbulence effects. For the genetic algorithm, individual beamlet's intensity could be varied asymmetrically to investigate if there is any significant improvement in the target peak irradiance and power-in-the-bucket rating. The genetic algorithm should be modified to search for the highest power-in-the-bucket instead the peak target irradiance, as that is a more significant parameter for predicting the DE weapon effectiveness.

A.1 Appendix

Table A-1. Approximate Laser Power Levels Needed to Affect Certain Targets
Multiple perspectives that may reflect varying assumptions about BQ and other factors

Source	Beam power measured in kilowatts (kW) or megawatts (MW)				
	~10 kW	Tens of kW	~100 kW	Hundreds of kW	MW
One Navy briefing (2010)	UAVs				
		Small boats			
				Missiles (starting at 500 kW)	
Another Navy briefing (2010)		Short-range operations against UAVs, RAM, MANPADS (50 kW-100kW; low BQ)	Extended-range operations against UAVs, RAM, MANPADS, ASCMs flying a crossing path (>100 kW, BQ of ~2)	Operations against supersonic, highly maneuverable ASCMs, transonic air-to-surface missiles, and ballistic missiles (>1 MW)	
Industry briefing (2010)		UAVs and small boats (50 kW)	RAM (100+ kW), subsonic ASCMs (300 kW), manned aircraft (500 kW)	Supersonic ASCMs and ballistic missiles	
Defense Science Board (DSB) report (2007)		Surface threats at 1-2 km		Ground-based air and missile defense, and countering rockets, artillery, and mortars, at 5-10 km	"Battle group defense" at 5-20 km (1-3 MW)
Northrop Grumman research paper (2005)	Soft UAVs at short range	Aircraft and cruise missiles at short range	Soft UAVs at long range	Aircraft and cruise missiles at long range, and artillery rockets (lower hundreds of kW) Artillery shells and terminal defense against very short range ballistic missiles (higher 100s of kW)	

Table A.1: Approximate Laser Power Level Needed to affect certain targets.
Source: [1]

THIS PAGE INTENTIONALLY LEFT BLANK

List of References

- [1] R. O'Rourke, "Navy shipboard lasers for surface, air and missile defense: Background and issues for congress," Naval Affair, WA, Tech. Rep. RL32665, Jun. 2015.
- [2] D. J. Richardson, J. Nilsson, and W. A. Clarkson, "High power fiber lasers: Current status and future perspectives," *J. Opt. Soc. Am. B*, vol. 27, no. 11, pp. B63–B92, Nov. 2010.
- [3] J. Hecht, "Half a century of laser weapons," *Opt. Photon. News*, vol. 20, no. 2, pp. 14–21, Feb. 2009.
- [4] (2010, July.). Kratos awarded 11 million contract to support the navy directed energy and electric weapon systems and total ship training system program offices. [Online]. Available: <http://www.globenewswire.com/news-release/2010/07/29/426352/197887/en/Kratos-Awarded-11-Million-Contract-to-Support-the-Navy-Directed-Energy-and-Electric-Weapon-Systems-and-Total-Ship-Training-System-Program-Offices.html>. Accessed Aug. 1, 2016.
- [5] W. Silfvast, *Laser Fundamentals*, 2nd ed. New York, NY: Cambridge University Press, 2004.
- [6] K. R. Cohn, "Free electron lasers in 2015," in *Proc. 37th International Free Electron Laser Conference (FEL2015)*, vol. Proc. FEL2015, 2015, pp. 625–629.
- [7] A. E. Siegman, "How to (maybe) measure laser beam quality," in *DPSS (Diode Pumped Solid State) Lasers: Applications and Issues*, Long Beach, CA, 1998, p. MQ1.
- [8] R. A. Motes and R. W. Berdine, *Introduction to High-Power Fiber Lasers*, 2nd ed. Albuquerque, NM: Directed Energy Professional Society, 2009.
- [9] E. J. Bochove, "Theory of spectral beam combining of fiber lasers," *IEEE JOURNAL OF QUANTUM ELECTRONICS*, vol. 5, no. 38, pp. 432–445, Aug. 2002.
- [10] D. R. Williams. (2016, May.). Earth fact sheet. NASA Goddard Space Flight Center. [Online]. Available: <http://nssdc.gsfc.nasa.gov/planetary/factsheet/earthfact.html>. Accessed Sept. 11, 2016.
- [11] P. Slater, *Photographic Systems for Remote Sensing*, 2nd ed., American Society for Photogrammetry, Falls Church, VA, 1985.
- [12] J. Schmidt, *Numerical Simulation of Optical Wave Propagation with Examples in Matlab*, 1st ed. Dayton, OH: Society of Photo-Optical Instrumentation Engineers (SPIE), 2010.

- [13] K. A.N, “The local structure of turbulence in incompressible viscous fluid for very large reynolds numbers,” *Proceedings: Mathematical and Physical Sciences*, vol. 434, no. 1890, pp. 9–13, July. 1991.
- [14] F. G. Gebhardt, “Twenty-five years of thermal blooming: an overview,” *Proc. SPIE*, vol. 1221, no. 2, p. 25, May. 1990.
- [15] D. C. Smith, “High-power laser propagation: Thermal blooming,” *Proceedings of the IEEE*, vol. 65, no. 12, pp. 1679–1714, Dec. 1977.
- [16] J. Goodman, *Introduction to Fourier Optics*, 3rd ed. Greenwood Village, CO: McGraw-Hill, 2004.
- [17] G. Tyler and D. Fried, “A wave optics propagation algorithm,” The Optical Sciences Company, California, CA, Tech. Rep. TR-451, 1982.
- [18] P. Roberts, “A wave optics propagation code,” The Optical Sciences Company, California, CA, Tech. Rep. TR-760, 1986.
- [19] (n.d.). Circles in circles. Stetson University. [Online]. Available: <http://www2.stetson.edu/~efriedma/cirincir/>. Accessed Aug. 22, 2016.
- [20] S. Coy. (n.d.). Wavetrain: A user-friendly wave optics propagation code. MZA Associates Corporation. [Online]. Available: <https://www.mza.com/publications/wtspiepaper.htm>. Accessed Sept. 1, 2016.
- [21] R. W. P. et al., *Thermal conductivity of selected materials*, 1st ed. U.S. Dept. of Commerce, National Bureau of Standards, 1966.

Initial Distribution List

1. Defense Technical Information Center
Ft. Belvoir, Virginia
2. Dudley Knox Library
Naval Postgraduate School
Monterey, California